CDC-NIOSH SBIR PHASE II FINAL REPORT
(Grant # *5 R44 OH007662-03, Aug. 2006 –Jan. 2009*)

A Non-Destructive Testing Consultant

A Laser-Based Devise for Work Site Stability Assessment

Xiaoqing Sun (PI), PhD. PE.
June Wang, MS and
Feng Guo, ME, MS.

AAC International
60 Mechanic Street
Lebanon, NH 03766-1521
Phone: (603)448-6177
Email: woodwall03@aol.com

April 2009

TABLE OF CONTENTS

LIST OF TERMS AND ABBREVIATIONS

ABAQUS – brand of a finite element simulation software package
AC – alternating current
AE – acoustic emission
AI – artificial intelligence
BSO – a type of photorefractive crystal ($Bi_{12}SiO_{20}$)
CPU – central processing unit
DC – direct current
FEM – finite element model or finite element method
MM – multi-mode
MSM – metal-semiconductor-metal structure
OFR – optical fiber amplifier
PI-EMF – Photo-induced electromotive force
RBI – reference beam interferometer
SAFELITE-1 – first generation optical AE mine monitor developed in this SBIR project
SAGNAC – a French physicist name, many optical devices are named by his name
SM – single mode
SMF – single mode fiber
TWM – two wave mixing
ZBLAN – short form for $ZrFM_4$-BaF_2-LaF_3-AlF_3-NaF

I. ABSTRACT

In 2006, the rate of occupational injuries and fatalities in the mining industry was 12 times higher than the national industrial average, and topped the list published by the Bureau of Labor Statistics (http://stats.bls.gov/news.release/cfoi.t02.htm). Based on the same statistics, the ratio of the number of reported accidents (including both fatal and non-fatal) to the total number of employees in the mining industry is as high as 1:10. The costs associated with these accidents have placed enormous economic burdens on families and the industry, as well as on society as a whole. Indeed, the impact of occupational injuries and fatalities goes far beyond economics. Tremendous effort will be necessary to reduce the rate of occupational injuries and fatalities and to ensure mine workers' rights to "safe and healthful working conditions" (Occupational Safety and Health Act of 1970). It is of great importance that technological, managerial and regulatory aspects of the industry be fully considered in this effort. In the new century, the mining industry will be challenged to provide its working men and women with safer and more healthful working conditions.

A laser-based acoustic emission (AE) detection device is proposed for work site structural stability assessment. This new device will take advantage of innovations in laser ultrasonics, artificial intelligence (AI), and advanced acoustic emission technology to provide mine workers with a unique, instant, real-time stability assessment of immediate rock structures in the working environment, which has not been attainable in the past. Nonlinear optical interferometry based on two-wave mixing and/or photo-induced electromotive force techniques will be used for AE signal detection from rock structures in mine sites. AI criteria will be established by wave pattern recognition to identify unstable areas in mine sites. This research will also result in a unique non-contact monitoring device for acoustic emission/microseismic studies, which will be very useful in many areas of application.

If the research and development is successful, the working men and women in the mining industry will have a convenient tool to check/ monitor safety conditions at their work sites and obtain sufficient time to take action before accidents occur. The innovation will reduce occupational injuries and fatalities caused by roof falls, sidewall crumples, stope collapses, slope slides, etc. in the mining industry.

The primary objective of the Phase II research is to develop the prototype of the AE detector and test it in real-world mining facilities. The primary objective consists of five major specific aims: 1. instrumentation development, 2. pre-field experiment preparation, 3. in-situ data collection, 4. AI criteria development, 5. system integration and in-situ trial.

This report documents the SBIR Phase II activity entitled "A Laser-Based Device for Work Site Stability Assessment" conducted by AAC International under Grant Number 2 R44 OH007662-02 and 5 R44 OH007662-03. The project was productive and fruitful, although it has not been completed because the amount of the actual work far exceeded original estimates. Significant progress was made toward the final project goal.

The concept for instrumentation of the proposed laser device for work site stability monitoring was demonstrated in the previous Phase I project. In the Phase II effort, the instrumentation was further refined into its prototype format suitable for field applications

through system optimization, miniaturization, and cost reduction. A digital audio AE monitor was also developed and tested, and was the first of its kind reduced into practice in the field. AE signal detection by laser instrumentation was tested on rock materials. It was found that weak signals caused by the low optical reflectivity of rock surfaces may seriously degrade the quality of the AE detection, and effort was therefore directed toward developing an optical fiber amplifier (OFA) for compensation. In preparation for field experiments on the stability monitoring system and failure criteria development based on acoustic emission, preliminary finite element models were constructed to study stress distribution around an underground longwall stope and to simulate AE activities generated in the rock structures. This established a framework for the analytical aspects of further development for field applications. In the system integration effort, the first generation mine AE monitor implementing the proposed laser-based AE detection concept, SAFELITE-1, has been assembled with major functions tested. At this stage, one of the key components of SAFELITE-1, the optical fiber amplifier, is still under development; thus, SAFELITE-1 is not yet fully prepared for field testing and failure criteria development.

II. HIGHLIGHTS/SIGNIFICANT FINDINGS

Research and development work was conducted to develop a laser-based device for work site stability assessment of mining structures, in order to provide mine workers with safer and more healthful working conditions. The concept of the proposed laser device for work site stability monitoring was demonstrated in the previous Phase I project. The primary effort in the Phase II project was to refine the instrumentation further into a prototype format suitable for field applications through system optimization, miniaturization, and cost reduction. This primary effort contains five major specific aims: instrumentation development, pre-field experiment preparation, in-situ data collection, AI criteria development, and system integration and in-situ trial.

Aim 1: Instrumentation Development. This specific aim involved three sub-tasks. The first sub-task was laser source optimization, in which laser sources, including a fiber laser and several inexpensive solid state lasers, were evaluated in order to determine which would replace the more expensive high-quality green laser used in the demonstration. Although no laser source was identified to replace the high-quality green solid state laser directly, experiments showed the possibility of using a low-powered solid state laser with an optical fiber amplifier for compensation.

The second sub-task was miniaturization of the TWM or PI-EMF device. In this sub-task, two small-sized interferometers, an improved PI-EMF device using Schottky MSM photo-detector and a SAGNAC interferometer were tested. However, it was found that neither will be able to match the performance of a TWM device. Then, effort was directed toward optimizing the fiber launching mechanism necessary for miniaturizing the TWM device.

The third sub-task was AE audio monitor development. A digital audio AE monitor was developed and tested, and was the first of its kind reduced into practice in the field.

Aim 1 extension: Development of Optical Fiber Amplifier. The studies in the first sub-task and Aim 2 indicated a key requirement of an optical fiber amplifier for success of this

development project. An OFA was studied and developed for 532 nm green light. The OFA uses Pr^{3+}/Yb^{3+} codoped ZBLAN fiber as a gain medium and 850 nm infrared as a pump. Initial success has been achieved. The OFA is still under development.

Aim 2: Pre-Field Experiment Preparation. This specific aim contains two sub-tasks: rock specimen preparation and trial AE signal collection using the improved laser device. Since at this time the prototype equipment has not been completed, limited work was conducted in testing AE data collection by using a TWM interferometer on rock surfaces. It was found that weak signal caused by low optical reflectivity of rock surfaces may seriously degrade the quality of the AE detection. Therefore, effort was further directed toward developing an optical fiber amplifier (OFA) for compensation as an extension of the work in Aim 1.

Aim 3: In-Situ Data Collection. As instrumentation of the AE detection is still underway, no activity has been carried out for Aim 3.

Aim 4: AI Criteria Development. In the first sub-task in Aim 4 work, to prepare for field experiments on the stability monitoring system and failure criteria development based on acoustic emission, preliminary finite element models were constructed to study stress distribution around an underground longwall stope and to simulate AE activities generated in the rock structures. This established a framework for the analytical aspects of further development for field applications.

The second sub-task in Aim 4 had no activity, because the instrumentation was not available.

Aim 5: System Integration and In-Situ Trial. In the system integration effort, the first generation mine AE monitor implementing the proposed laser-based AE detection concept, SAFELITE-1, has been assembled with major functions tested. At this stage, SAFELITE-1 has not been completed for field tests and failure criteria development, because one of its key parts, the optical fiber amplifier, is still under development.

III. TRANSLATION OF FINDINGS

The ultimate goal of this SBIR project is to develop a handheld device for instant, real time stability assessment of immediate rock structures and support systems at the work site. This directly addresses the occupational safety needs of the nation's 200,000 miners. If the research and development is successful, the working men and women in the mining industry will have a convenient tool to check and/or monitor the safety conditions at their work sites and learn of potentially dangerous conditions with sufficient time to withdraw before accidents occur.

At this time, the first generation prototype equipment, SAFELITE-1 is close to complete. This equipment will provide the mining industry and government agencies a powerful tool in occupational safety assurance to ensure miners' rights to "safe and healthful working conditions" (Occupational Safety and Health Act of 1970). This will constitute great societal benefit to the mining population as well as the country.

IV. OUTCOMES/RELEVANCE/IMPACT

1. The primary outcome of this project will be an optical AE mine monitor, SAFELITE-1. It should be classified as potential outcome, because it is still under development.

Mine structures are geometrically complex and subject to various overburden and tectonic pressures. The work sites of miners are usually under complicated stress conditions. The immediate rock structures, such as roofs, sidewalls, and working faces at work sites, are frequently overstressed unbeknownst to the operating crew, which exposes the personnel to potential professional injury. The recent tragedy at Crandall Canyon Mine, UT (August, 2007), which claimed 9 lives and shocked the entire nation, is just one of the examples. SAFELITE-1 will be able to locate the over-stressed locations in mining structures by detection of AE activities and help miners to reduce the exposure to professional injury and fatality at work site.

2. The digital audio AE monitor is an intermediate outcome generated in the process of SAFELITE-1 development. The digital audio AE monitor uses the multimedia functions of modern computing technology to replace the low quality heterodyne audio monitors. This is its first implementation in the field. The digital audio AE monitor will be used in SAFELITE-1. The concept will also facilitate acoustic emission research in mining and other related engineering areas.

3. FEM models for AE simulation in rock structures is developed in preparation for field work in SAFELITE-1 development. This is an intermediate outcome that will assist theoretical studies of acoustic emission activity in mining and other engineering areas.

4. The 532 nm optical fiber amplifier (OFA) developed in this project is still being optimized and tested, although initial success has been achieved. The OFA will be used in SAFELITE-1.

V. SCIENTIFIC REPORT

Part 1: DURATION OF THE SBIR PHASE II PROJECT

This report documents the Small Business Innovation Research (SBIR) Phase II effort entitled: "A Laser-Based Device for Work Site Stability Assessment" conducted by AAC International, Lebanon, NH under Grant Number 2 R44 OH007662-02 and 5 R44 OH007662-03 from the National Institute for Occupational Safety and Health, Centers for Disease Control and Prevention between August 17, 2006 and July 31, 2008 with a one-half-year no-cost extension granted to January 31, 2009. The purpose of the research was to develop a prototype of a laser-based device for work site stability assessment used in mining operations.

Part 2: PERSONNEL UTILIZATION

The personnel worked on the project during this project period include:

Name	Title	Dates of Service	Hours Worked
Dr. Xiaoqing Sun	PI	8.16.2006 – 1.31.2009	4348
Dr. Hongxin Bian	Senior Scientist	11.15.2007 – 1.31.2009	160
Ms. June Wang	Staff Engineer	8.16.2006 – 1.31.2009	4296
Mr. Feng Guo	Staff Engineer	11.15.2007 – 1.31.2009	2280
Mr. Robert Silliman	Engineering Aid	9.1.2006 – 12.15.2007	80
Mr. L. Raymond Sun	Secretary	9.1.2006 – 8.31.2007	768
Dr. William Sun (Northrop Grumman Co.)	Consultant	7.17.2007 – 10.31.2008	500
Dr. Wei Xu (StockerYale Inc.)	Consultant	3.1.2008 – 12.31.2008	480
Dr. Ming Dao (Massachusetts Institute of Technology)	Consultant	9.1.2006 – 9.30.2006	80

Part 3: PHASE II SPECIFIC AIMS

The objective of this SBIR project is to develop a laser-based non-contact acoustic emission (AE) monitoring device for worksite stability assessment. A successful development of non-contact hand-held monitoring may effectively locate potential failure (roof falls, sidewall crumples, slope slides and supporting system failures) of immediate rock structures; and reduce occurrences of professional injuries in the mining industry. The proposed concept draws on significant advances in industrial non-contact nondestructive testing in recent years, and will contribute to providing mine workers with a safer and more healthful working environment. The previous Phase I study successfully demonstrated the feasibility of the proposed concept. Six specific aims are involved in this subsequent Phase II development. They are: instrumentation development, pre-field experiment preparation, in-situ data collection, AI criteria development, system integration and in-situ trial, and documentation and reporting.

Aim 1: Instrumentation Development

Develop and optimize the instrumentation of the laser-based AE monitor based on results from the previous Phase I research. This aim contains three sub-tasks:

Sub-Task 1.1 Laser source optimization.
Sub-Task 1.2 Miniaturization of TWM (PI-EMF) Device.
Sub-Task 1.3 Digital Audio AE Monitor.

Aim 2: Pre-Field Experiment Preparation

Prepare for in-situ data collection with the instrumentation developed in Aim 1. Two sub-tasks are involved:

Sub-Task 2.1 Rock specimen preparation
Sub-Task 2.2 Trial AE signal collection using the improved laser device

Aim 3: In-Situ Data Collection

Collect in-situ acoustic emission data from various mining structures in selected mines for further AI function development. Information on geologic conditions of each selected mining structure will also be collected in order to build finite element models to be used in Sub-Task 4.1.

Aim 4: AI Criteria Development

Build criteria for instability development inside the rock structures based on the acoustic emission waveforms collected from the mining structures. Finite element model (FEM) will be used to describe stress conditions (or instability development) for criteria development. Two sub-tasks are involved in this effort:

Sub-Task 4.1 FEM analysis on underground testing structures
Sub-Task 4.2 AE waveform feature classification

Aim 5: System Integration and In-Situ Trial

Integrate the prototype laser-based device by using the hardware developed in Aim 1 and software developed in Aim 4. Test the prototype in situ at operating mining facilities.

Aim 6: Documentation and Reporting

Document the entire research and development work conducted under this SBIR Phase II project. Prepare necessary reports to meet the requirements of CDC-NIOSH grant management.

The progress of the proposed research and development is shown in Figure 1.

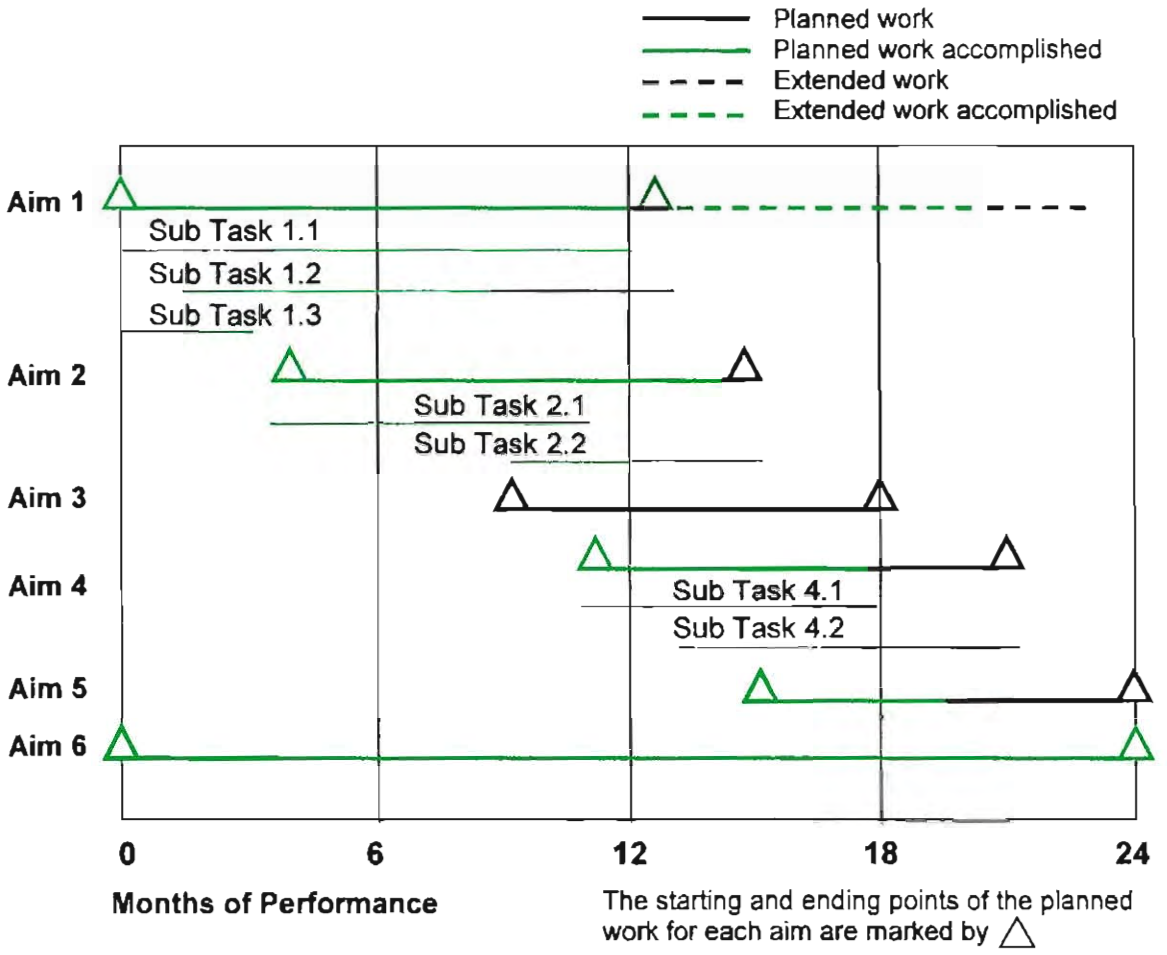

Figure 1 Performance summary of the SBIR Phase II Work

Part 4: PROGRESS AND RESULTS

The entire Phase II project has been directed toward development of the laser-based acoustic emission monitoring device for worksite stability assessment, as outlined in the proposal. The effort generally follows the proposed specific aims listed in Part 3. The project was productive and fruitful, although has not been completed due to the amount of the actual work was far beyond the original estimates. Significant progress was made toward the final project goal. The following sections will discuss the progress and results obtained for each of the specific aims.

4.1 Aim 1: Instrument Development

Instrumentation development for the proposed laser device for worksite stability monitoring involves a laser interferometer-based AE sensing unit, conventional AE signal conditioning, and PC-based data acquisition and analysis. In the Phase II effort, the instrumentation was further reduced into its prototype format suitable for field applications. Further system optimization, miniaturization and cost reduction were the three key objectives in the instrumentation

development. The effort in Aim 1 was divided into three sub-tasks: laser source optimization, miniaturization of TWM (PI-EMF) device, and digital audio AE monitor. The work in Aim 1 The work was also extended to develop an optical fiber amplifier, a key element for successful application of the interferometry sensing unit to rock surface monitoring.

4.1.1 Sub-Task 1: Laser Source Optimization

As discussed in the original Phase II proposal, laser source optimization involves several aspects: 1. optical path compensation [Fan, 1996], 2. fiber laser adoption, and 3. market exploration.

1. Optical Path Compensation. Suppose the optical path difference between the two legs (signal beam and reference beam) of a reference beam interferometer (RBI) is Δl, and the frequency noise is ν. In practice, Δl can be divided in two parts: one, Δl_s, is the physical difference between the optical paths (static), the other, Δl_{ult}, is the difference caused by acoustic surface movement on the signal leg. The output, P_{out}, from the RBI can be expressed as [Fan, 1996]:

$$P_{out} \sim 1 + \cos\left(\frac{2\pi \cdot \upsilon \cdot \Delta l}{c}\right) \qquad \text{(Eq. 1)}$$

At a proper bias point $2\pi\nu\Delta l/c = m\pi/2$, where m is odd, the output $P_{out} \sim 1 + \nu\Delta l = 1 + \nu\Delta l_s + \nu\Delta l_{ult}$. The influence of frequency noise may be reduced by elimination of $\nu\Delta l_s$. This can be done by compensating the shorter leg in the RBI, so that the static lengths of the two legs are equal. This can also reduce the influence of fluctuation of laser source to ensure detection of a clean acoustic signal.

Optical path compensation is an improvement on the structure of optical path which will be implemented during the assembly of the optical instrumentation, when exact length of signal beam is finalized.

2. Fiber Laser Adoption. Fiber laser adoption is to study the feasibility of using fiber laser in improving the frequency stability of the laser source.

In this direction, originally two types of fiber laser were examined in detail. One is based on double clad rear earth (ytterbium)-doped silica fiber. The other type of fiber laser uses holmium-doped fluoride glass fiber (ZrFM4-BaF2-LaF3-AlF3-NaF or ZBLAN). In the ytterbium-doped silica fiber laser, a 915 nm laser diode is used as pump to generate laser emission at 1120 nm. A PPLN crystal is used as frequency doubler to obtain the second harmonic at 560 nm (green). MPB Communications, Inc., of Montreal, Canada, provides such fiber laser module as a commercial product. Arrangements were made to conduct experiments for evaluation at AAC by

Figure 2 Green fiber laser (MPB VFL-P-1W) used in the evaluation

using their demonstration unit in mid-June of 2007. Figure 2 shows a photograph of the unit. This fiber laser unit represents a very typical fiber laser in the current market, which grew out of telecommunications applications. The major parameters of the fiber laser are listed below:

Model number: VLF-P-1-560
Output power: 1 watt
Emission wavelength: 560 nm
Transversive mode: TEM_{00}
Polarization: linear
Long term wavelength stability: 0.02 nm
Emission line width: <0.08 nm
Beam diameter: 0.5 mm @20 mm from output window
Beam divergence: <5 mrad

The tests of fiber laser were conducted on the two-wave mixing device used in the proposed AE monitoring instrumentation. Its optical setup is shown in Figure 3. A laser (in this case, MPB VFL-P fiber laser as discussed above) is used as the optical source in Figure 3. The wave plate, WP0, and the polarized beam splitter, PBS_0, are used to adjust the optical power injected into the interferometry system. The following wave plate – beam splitter set (WP1 and PBS_1) divides the laser source into a pump beam and a signal beam. The s-polarized signal beam is

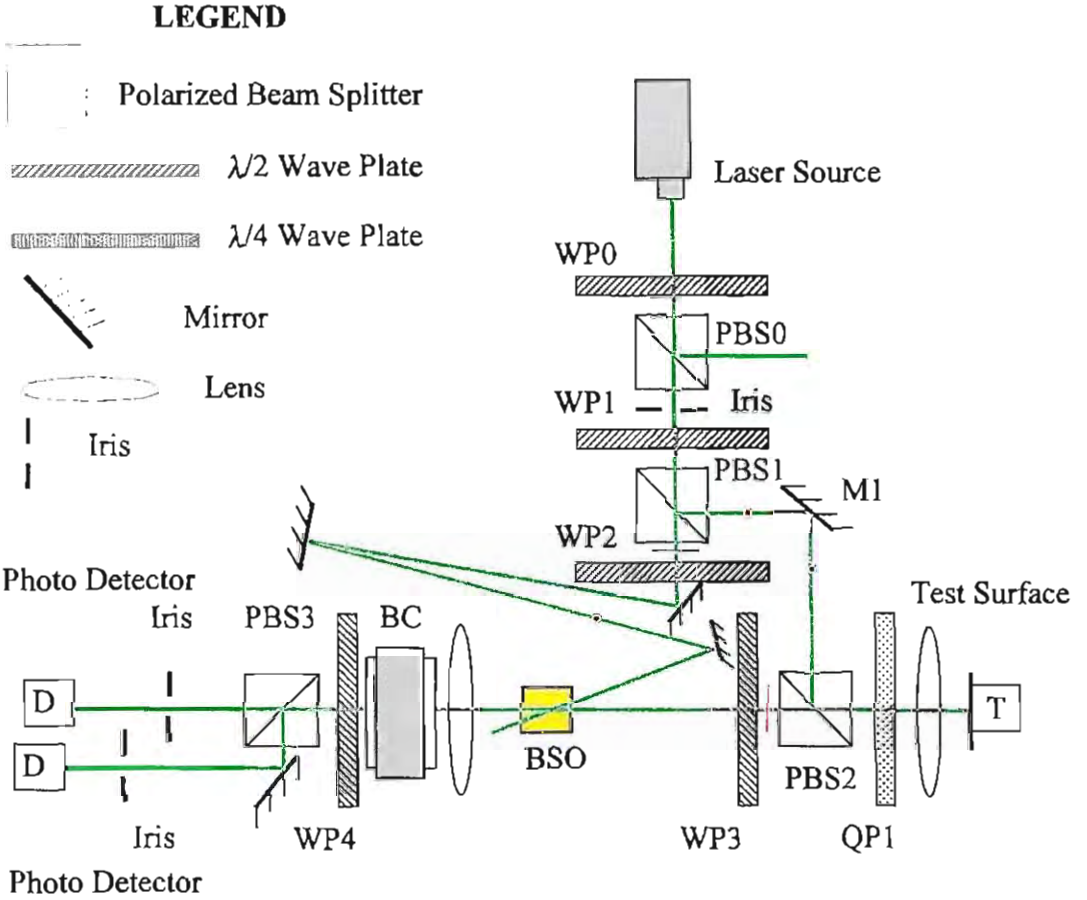

Figure 3 Optical setup for two-wave mixing based acoustic emission detection

directed to PBS_2 by mirror M1, and then reflected to the surface of the test specimen through a quarter wave plate, QP1, and a lens set. Then the signal beam is reflected from the specimen surface. The lens set collects and collimates the reflected signal beam and sends it back to PBS_2, through which the signal beam is projected to the photorefractive crystal (BSO). The half wave plate, WP3, is used to rotate the polarization of the signal beam to 45° from vertical axis, creating both s- and p-polarized components. The polarization of the p-polarized pump beam after PBS_1 is rotated by WP2 to the s-direction and interferes with the s-polarized component of the signal beam at the BSO, creating photorefractive gratings on which the beams are diffracted and energy transfer occurs in the usual two-wave mixing sense. The BSO crystal is oriented with grating vector along the [001] crystal axis, and a sinusoidal electric field of 6 KV/cm at 3200 Hz is applied to enhance the diffraction efficiency.

For simplicity of discussion, optical activity inside the BSO crystal is not included in the description; the details of the optical phenomenon may be found in Zhou [2004]. At the output of the BSO, the diffracted reference beam (which is wave front matched with the signal beam) and the transmitted signal beam are collected. The p-polarized component of the signal beam is then phase-delayed with respect to the s-polarized reference beam using a Berek compensator (BC). The phase shift is chosen such that interference occurs at the quadrature point in order to maximize the detection sensitivity. The wave plate (WP4) and beam splitter (PBS_3) allow for the combination of the polarization components at the balanced detectors. The detectors, using a differential amplifier to suppress the optical noise, generate electric analog signals for the acoustic emission signals detected at the test specimen [Murray and Krishnaswamy, 2001].

During the assembly of the TWM sensing unit, two improvements were made to the existing TWM setup. The first was to increase the waist diameter of the laser beam to approximately 5 mm to make full use of the photorefractive crystal to increase the two-wave mixing gain. The second was to use front surface mirrors to reduce the noise caused by double reflection induced by conventional back-doped mirrors. Significant quality improvement was observed after these changes.

Figure 4 is a photograph of the fiber laser (MPB VFL-P-560) used as light source of the TWM interferometry for acoustic emission detection.

Figure 5 shows the comparison of acoustic emission signals detected by using high quality solid state laser and by using the fiber laser as the light source. The AE signal was generated by a piezoelectric pulser with center frequency at 1 MHz, which possesses excellent repeatability for the purpose of comparison. The AE signal shown in Figure 5a is detected by using a high quality solid state laser as light source. Figure 5b shows the signal detected by using fiber laser as the source. It is obvious that detection by using the fiber laser pumped TWM unit was not able to generate a reasonable output. The appearance of spontaneous fictitious signals in Figure 5b indicates that the fiber laser involved multiple emission wavelengths or lines spanning over the 0.08 nm (115 GHz) band width beating each other at interference. This phenomenon seriously degraded the quality of AE signal detection. In the use of interferometry, although a broader line width might be tolerated, the monochromaticity of the light source is a prerequisite; therefore, enthusiasm for using fiber laser is discouraged. Further study on improving the quality of the fiber laser is beyond the scope of this applied research. As a result, the attempt to use holmium-doped ZBLAN fiber laser has been suspended.

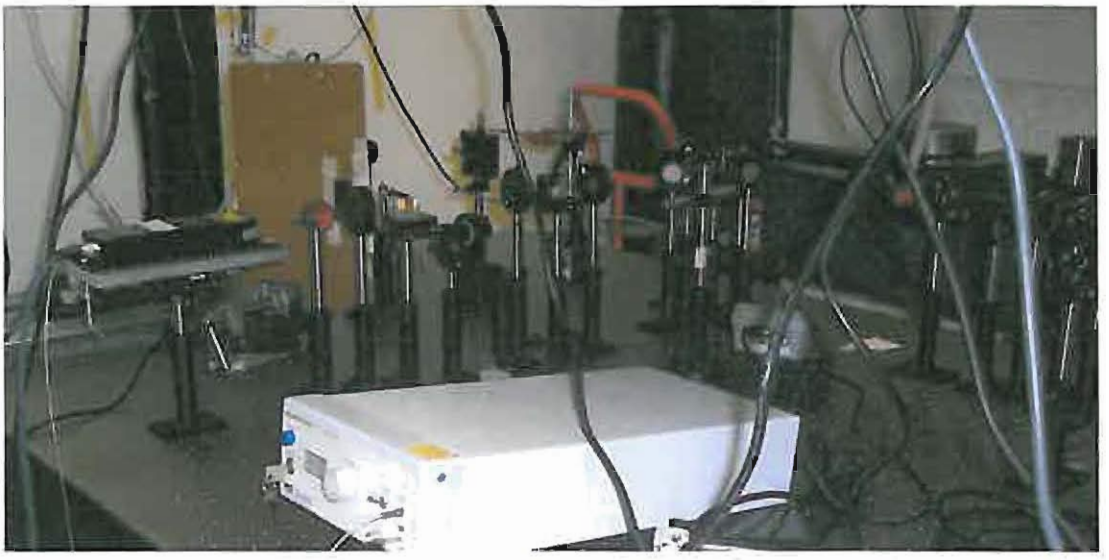

Figure 4 Photograph of testing fiber laser (MPB VFL-P) on TWM sensing unit for acoustic emission detection

a. TWM output using solid state laser source (LIGHTWAVE 142H)

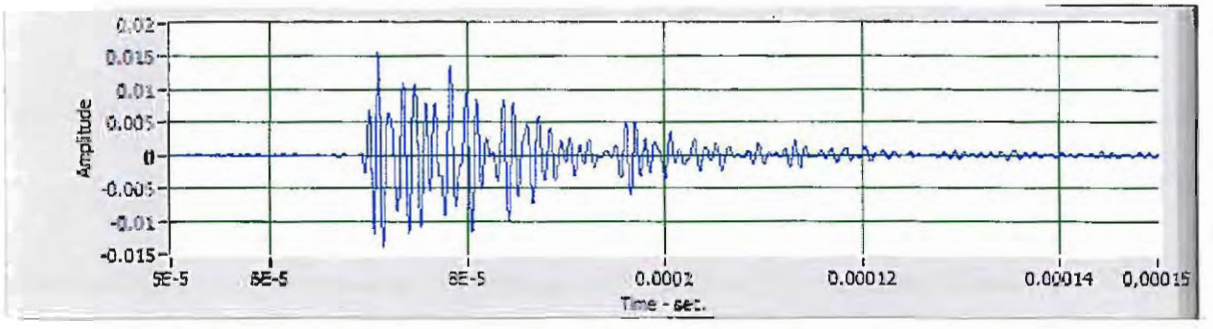

b. TWM output using fiber laser source (MPB VFL-P 560)

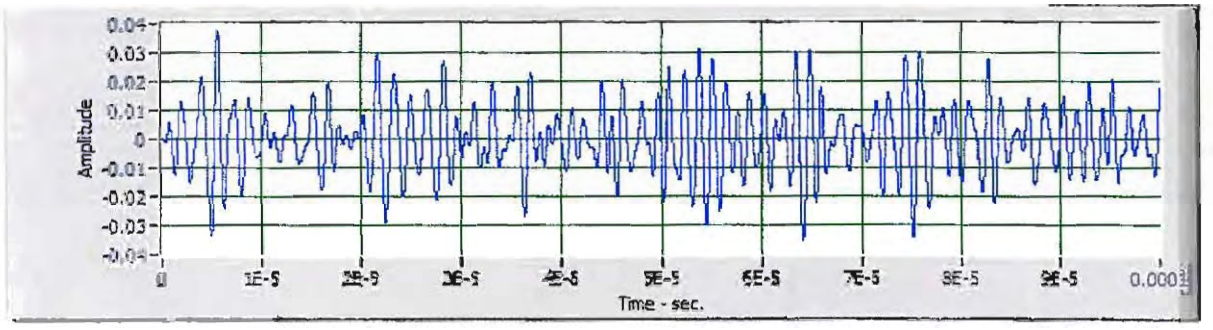

Figure 5 Comparison of fiber laser pumped TWM AE detector with solid state laser source pumped TWM detector (pulser generated AE signal with 1 MHz center frequency).

3. Market Exploration. Although a large amount of effort has been directed to fiber laser study, it is not considered the only option for instrumentation improvement. As discussed in the Phase II proposal, the purpose of laser source optimization is to find a laser not only with best frequency stability, but also relatively economical. For this reason, extensive market exploration was conducted to find a laser source similar to but less expensive than the one used for the Phase I feasibility demonstration. In this effort, several solid state lasers were identified and tested. These include: Model LLS-532-NH-1000-1 from Laserglow.com ltd.; Slim-532-300mw of Oxxius; and GMLN-532-100EC from Lasermate Group, Inc. Figure 6 shows a typical solid state laser used in this effort. The lasers were tested on the TWM experimental setup as shown in Figure 3. The photograph of experimental setup for the evaluation test is shown in Figure 7.

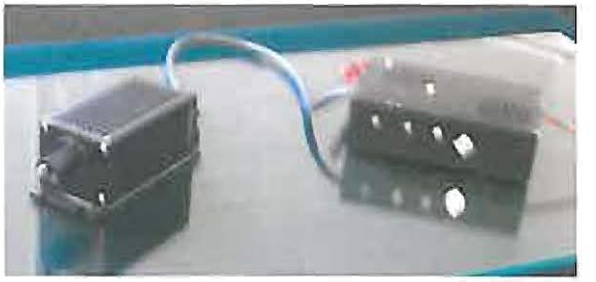

Figure 6 Typical inexpensive solid state laser tested for TWM AE detection unit

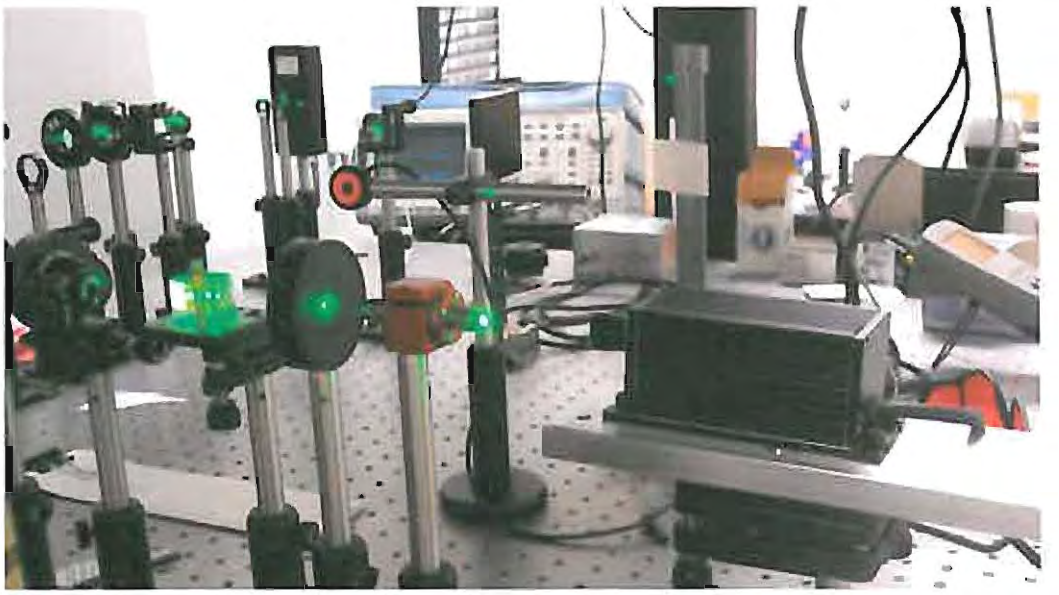

Figure 7 Experimental setup for evaluation of solid state laser sources for TWM base acoustic emission detection

Figure 8 shows the AE signal detected by using these economical solid state lasers. The AE signals were generated by using a piezoelectric pulser with center frequency at 1 MHz. Compared with the signal detected by using the high quality laser source, as shown in Figure 5a, the AE signal detected by using economical laser sources seemed competent. However, the signal detected was noisier than the one shown in Figure 5a, because the AE signal detected by using the cheaper laser sources as shown in Figure 8 requires multiple averaging (3 – 10 samples with the larger number of samples required by higher power modules) while the AE signal using high quality laser source (such as LIGHTWAVE 142H) does not. This might be due to the unstable optical frequency of the cheaper laser sources, reflected by unstable phase shift during the test measurement. Another significant drawback of the cheaper lasers is the unstable thermal property that creates random noises that are difficult to overcome. This drawback becomes more

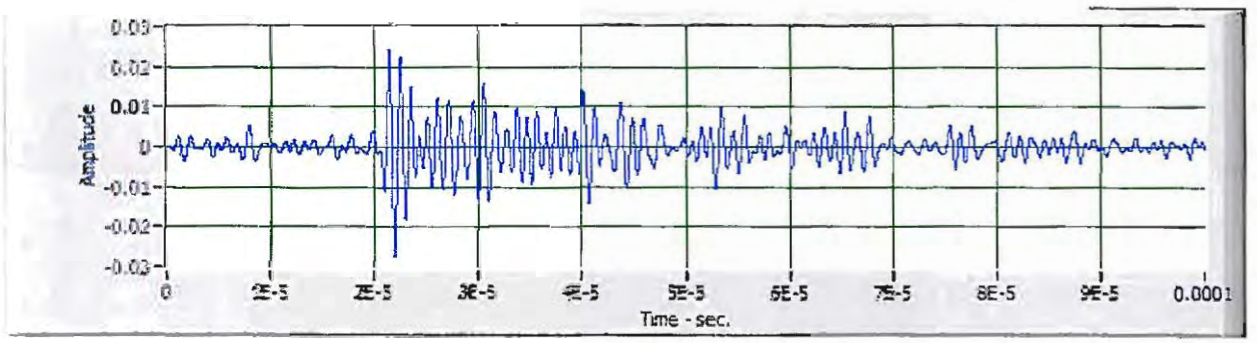

Figure 8 Output of TWM AE detector pumped by economic solid state laser source (piezoelectric pulser-generated AE signal with center frequency at 1 MHz).

significant when the power of the laser is above 150 mW, while the TWM device performs better with a high powered pump source (300 – 500 mW).

A variety of different laser sources has been tested for TWM interferometry in the AE signal detection application. In these trial tests, the solid state laser LIGHTWAVE 142H, as used in the Phase I feasibility demonstration, performed better than all the other lasers tested. Therefore, this laser source will be used for further system integration of the prototype equipment in order to obtain the best technical performance of the prototype, which is very important at this stage. Fiber laser source did not show great promise in the trials because of its multi-line nature of the spectrum, in addition to the fact that the spectral width of fiber lasers is much broader than that of LIGHTWAVE 142H. Since the evaluation involved only one fiber laser unit (MPB VFL-P), it is not clear whether this multi-line spectral nature is a property of this particular unit or a general characteristics of all fiber lasers induced by the lasing mechanism. Even if the fiber laser can be strictly monochromatic, its current cost is almost comparable to the high quality solid state lasers, such as LIGHTWAVE 142H. *Therefore, the use of fiber laser is not motivated at this time.* In the case of inexpensive solid state lasers, reasonably good performance may be obtained at low power modules (< 100 mW). In order to compensate the beam intensity during detection, an optical amplifier may be used. This provides an alternative to the expensive high quality laser source, costing only 30% of the cost of high quality laser sources such as LIGHTWAVE 142H. This is very attractive for the product commercialization stage. The necessity for use of optical amplifier arises from another aspect of the application, which will be discussed in Section 4.2.2.

4.1.2 Sub-Task 1.2: Miniaturization of Laser Device

A major effort in the instrumentation development is to reduce the free-space setup into portable format so that it can be conveniently carried around in field application. In miniaturization, we continued to work on the two most promising nonlinear devices for acoustic emission signal detection. One applies TWM technique for ultrasonic/acoustic sensing and the other utilizes PI-EMF technology [Pepper, 1997]. Both were demonstrated in the previous Phase I study for AE signal detection. In this sub-task these devices were further studied in order to reduce the size and weight, and enhance the performance for field applications. In addition, an all-fiber laser device, Sagnac interferometry, was also studied for the potential application because of its ultra-light weight and small size.

1. Sensing unit using PI-EMF device. The photo-current modulated at frequency Ω that is produced in a cubic photorefractive crystal with average photo-conductivity σ_0 is described by M. P. Petrov, et al. [1990]:

$$j(t) = \frac{m^2 \Delta}{4}\sigma_0 \frac{K V_{th}}{1 + K^2 L_D{}^2} \frac{(-j\Omega)}{\Omega_c + j\Omega} \exp(i\Omega t)\, S \qquad \text{(Eq. 2)}$$

The parameters in this equation are as follows:

m is the optical modulation depth: $m = 2\sqrt{I_0}\sqrt{I_1}/(I_0+I_1)$ and
I_0 and I_1 are the intensities of the two optical beams that interfere in the crystal.
$\Delta = k\,\delta L$, where $k = 2\pi/\lambda$ and
λ is the wavelength of the laser light in air and
δL is the depth of vibration of the ultrasonic wave.
$K = 2\pi/\Lambda$, where Λ is the grating spacing: $\Lambda = \pi/k\sin\theta = \lambda/2\sin\theta \approx \lambda/2\theta$, and
θ is the angle of the incident beam from the normal, and
2θ is the angle between the two beams.
V_{th} is the thermal voltage at room temperature $= (k_B T/e) = 0.026$ mV.
L_D is the diffusion length in the material.
$\Omega_c = [\tau_M(1 + K^2 L_D{}^2)]^{-1}$ where τ_M is the dielectric relaxation time of the crystal, and
$\tau_M = \varepsilon/\sigma_0$, where ε is the dielectric permittivity of GaAs $= 13\ \varepsilon_0$, and
ε_0 is the dielectric permittivity of free space: 8.85×10^{-14} F/cm.
S = the lateral area over which current density is generated = W d, where
W = width of illuminated electrode region
d = depth down from the surface of the photo-current region

This description laid the foundation for a group of reference beam interferometers using photo-induced electro-motive force (PI-EMF) caused by the varying interference pattern of two laser beams. The PI-EMF based sensing unit was initially chosen as the primary method because of its simplicity and low cost. It does not require many polarizing beam splitters and balanced detectors, as are required by the two-wave mixing method. At the same time, however, it does require an amplifier with high sensitivity.

In the previous Phase I study, a PI-EMF sensing unit was tested. The test used AE signals generated both by pencil break and piezoelectric transducer. The AE signals were detected in the experiments. A more detailed study in this direction found that the responsivity of GaAs crystal is only 7.4×10^{-9} A/W. In order to increase the responsivity, we imposed a 5v bias voltage across the photorefractive crystal. This achieved a corresponding responsivity of 1.2×10^{-6} A/W. Figure 9 shows the result obtained from the test specimen with improved sensing responsivity as a result of using a piezoelectric transducer as the AE source. Figure 9b is the AE signal monitored with a PI-EMF interferometer. Figure 9c is the signal from a reference piezoelectric transducer (conventional sensor). Since the location of the sensing point is different for each transducer, the signals detected from the test are not exactly the same; however, they are quite close. Approximately 150 mW optical power was used for each of the reference and signal beams. The signal-to-noise ratio of the PI-EMF unit is around 20 dB.

a. Output from MSM GaAs photo diode

b. Output from single GaAs crystal

c. Output from narrow band piezoelectric transducer

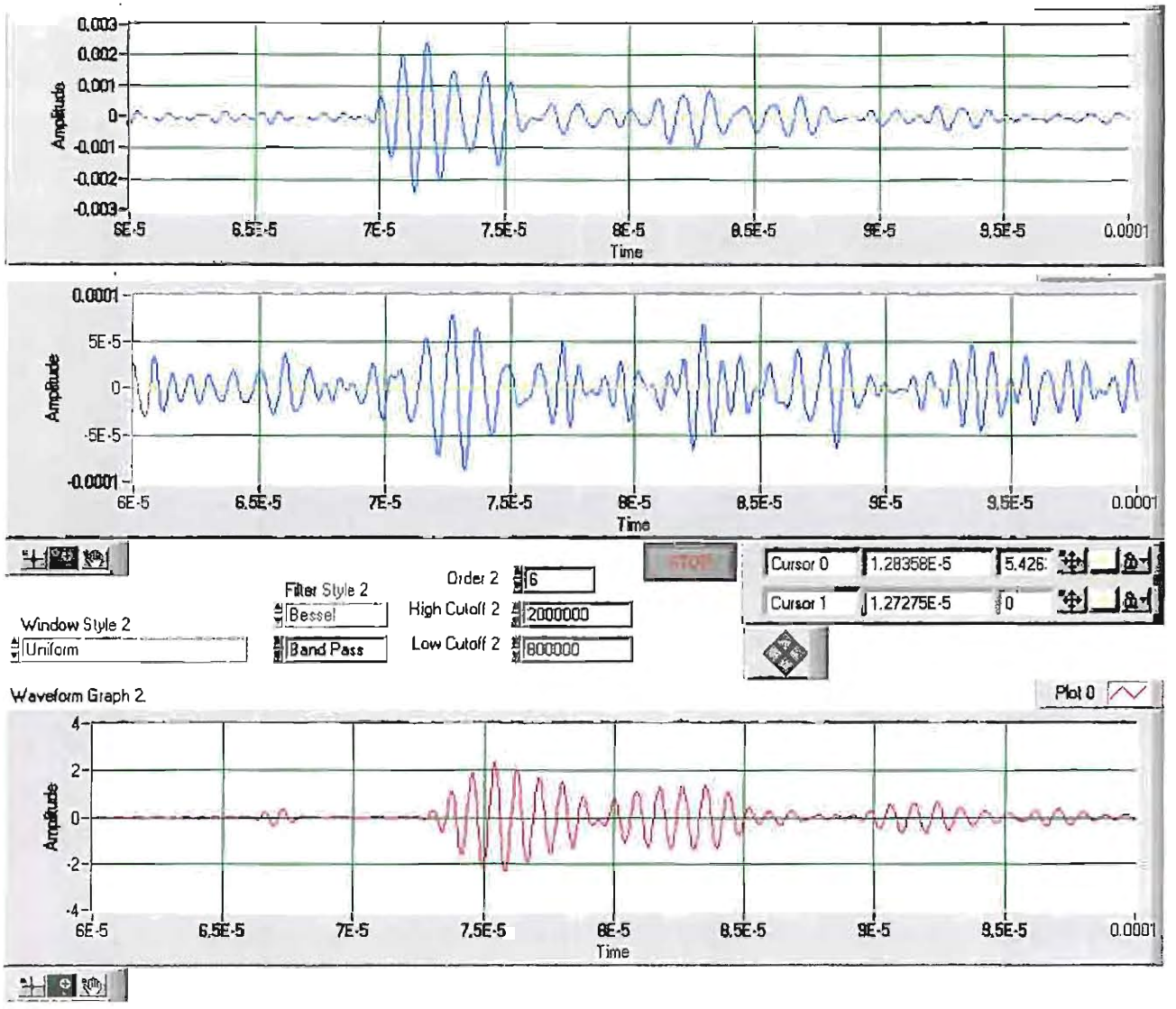

Figure 9 Comparison of AE signals collected by MSM GaAs diode and GaAs single crystal

In the Phase I research, we were able to construct a Photo-EMF interferometer device, and obtained initial results as it was used for acoustic emission signal acquisition. The improved responsivity of GaAs (1.2×10^{-6} A/W) appeared very low for a reasonable measurement in the proposed application. Theoretically, there are two ways to further increase the responsivity of the PI-EMF unit: One is to increase the incident optical power on the crystal so that more electrons can be generated in it, and the other is to increase the contact between the electrodes and the photorefractive material so that more electrons can be caught during the photonic process. In the Phase II research, in an effort to further improve the sensitivity of the PI-EMF unit, a photo diode (G4176) from HAMAMATSU was obtained. This diode uses symmetrical interdigital Schottky contacts to increase the contact area between the electrodes and the material of GaAs crystal. It is the first-ever MSM (metal-semiconductor-metal) photo detector made on GaAs. It is made by HAMAMATSU for communication applications. Although its sensing area is relatively small ($200\mu m^2$), it is able to bring the responsivity to 0.2 A/W at 532 nm wavelength for GaAs, which is quite attractive for the proposed application. The previous tests on the PI-EMF unit used a simple reference beam interferometer. Although that is the commonly accepted assembly for the PI-EMF unit, during the experiment it was difficult to narrow the angle between the signal beam and reference beam to less than 1.5° due to the finite size of the mirrors involved, while theoretically 0° will generate the best interference pattern. In the Phase II study, the configuration of a Michelson interferometer was adopted to achieve the ideal 0° angle between signal and reference beams, as shown in Figure 10.

In the Michelson interferometer setup, the laser beam is split equally into signal and reference beams by a half-wave plate (WP1) and a polarizing beam splitter (PBS1). The reference beam is reflected by a fixed mirror and projected to the G4176 photo diode. The signal beam is directed to the test surface and reflected back through the polarizing beam splitter to the photo diode. It then interferes with the reference beam at the G4176 photo diode. The quarter wave plates (QP1 and QP2) are used to control the direction of the laser beams in the optical

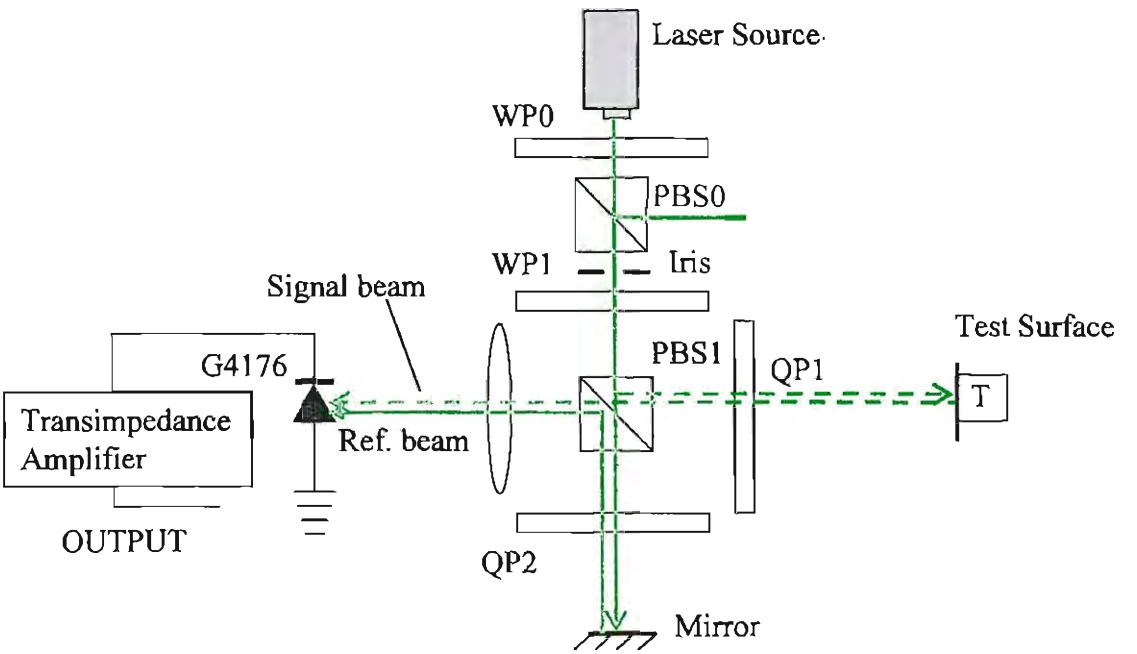

Figure 10 Optical setup for Photo-EMF using Michelson interferometer

setup. The half-wave plate, WP0, and another polarizing beam splitter, PBS0, are used to adjust the total laser beam intensity for the interferometry. The transimpedance amplifier then converts the interference pattern on the photo diode into electric analog signals of the acoustic emission at the test surface.

Figure 11 Photograph of PI-EMF device using Michelson configuration

Figure 11 is a photo of the PI-EMF device using the Michelson configuration. Figure 12 is a closer look at the photo diode (G4176) and transimpedance amplifier. The results of AE detection by MSM GaAs are also plotted in Figure 9 for comparison purposes. The output from the MSM GaAs diode (Figure 9a) is greatly improved as compared with the result from the single GaAs crystal (Figure 9b), in terms of both signal to noise ratio and sensitivity. The result is almost comparable with that from the TWM unit. However, when the signal beam is directed to a rough test surface for AE detection, the quality of the signal collected will seriously degrade. A possible explanation is that the nonlinear compensation for rough surface effects by PI-EMF requires a sensory element of a certain size. The Schottky electrode of the photo diode, although it increased the dimensions of contact between electrodes and the photorefractive material, significantly reduced the area in between the electrodes, particularly the distance between the electrodes,

Figure 12 MSM GaAs photo diode with transimpedance amplifier

which is crucial for nonlinear compensation. The TWM unit, on the other hand, showed much better sustainability under rough surface conditions. It appeared that the TWM device was superior to the PI-EMF unit.

2. *Sagnac Interferometry.* SAGNAC effect was first observed by French physicist Georges Sagnac in 1913. It states that two identical light beams traveling in opposite directions around a closed loop path experience phase difference, when the loop is rotated about its normal axis, and this phase difference is proportional to the rotation rate. In the SAGNAC interferometer, the two light beams in a loop originate from a source external to the loop. After one transit around the loop, they are extracted from the loop and recombined so that they interfere and produce a fringe pattern. When the device is rotated, the SAGNAC phase shift results in a shift in the fringe pattern. This variation may be monitored by a suitable photo-detector, which is a measure of the rotation rate. SAGNAC interferometer has been used in aerospace industries for gyroscope applications, which brought revolutionary improvement in aviation navigation. When used in ultrasonic or acoustic emission signal detection, the phase shift is not derived from the device rotation; rather it is caused by movement of the testing surface induced by ultrasonic or acoustic emission signals.

Figure 13 shows a SAGNAC interferometer used for acoustic emission signal detection in this study. Its basic mode of operation is as follows. The light from a SLD laser source (SUPERLUM 371-MP 830 nm) is passed through an isolator, PM_1, and a polarizer, and amplitude divided at a 50:50 directional coupler (PM_2) to follow the clockwise and counter-clockwise paths in the SAGNAC loop. The loop is interrupted near one end by a coupler (PM_3). The light is projected to the test surface and then reflected back to and collimated by the collimator. Then the lights continue to traverse the remaining paths (both clockwise and counter-clockwise) and recombine at the photo-detector. The intensity of the interfered beams is give by the following [Carolan et al, 1997]:

$$I = I_0[1 - V_i \cos(\phi + \phi_d)] \approx A + BI_0\phi_d \qquad \text{(Eq. 3)}$$

where I_0 is a constant intensity of the input light, V_i is the fringe visibility, ϕ is the phase difference between the two beams when the target is stationary, ϕ_d is the phase difference between the two beams, which is proportional to the change of displacement of the test surface

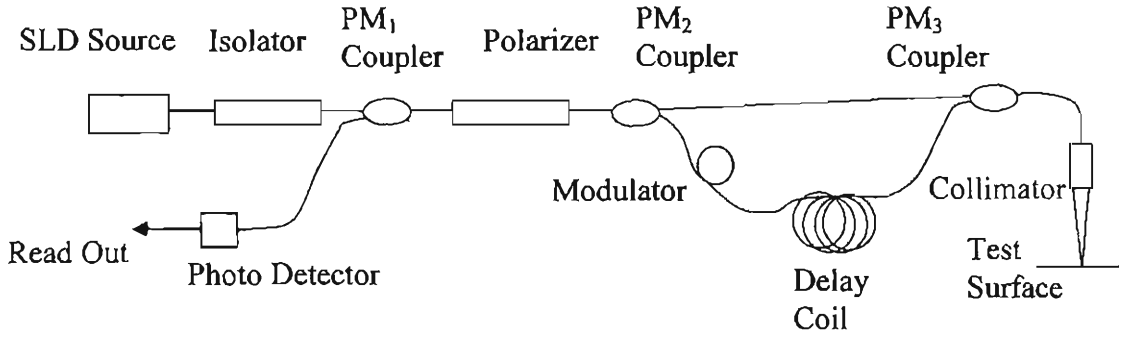

Figure 13 SAGNAC interferometer used for ultrasonic signal detection (PM version)

caused by the acoustic disturbance. During acoustic emission measurement, $A = I_0(1 - V_i \cos\phi)$ and $B = V_i \sin\phi$ are system constants. Equation 3 establishes the linear relation between the intensity of the interfered beam and the acoustic emission displacement on the test surface.

Thus, the readout from the photo-detector will reflect the change of the interference pattern of the two beams, i.e. the AE displacement. The entire setup is constructed using optical fiber. It is truly path matched and does not require active stabilization. The system is compact, small and easy to carry around. The SAGNAC interferometer shown in Figure 13 used polarization maintaining (PM) fiber for the optical paths, intended to increase the stability of the optical performance. Figure 14 is a photograph of the PM fiber based SAGNAC interferometer constructed at AAC.

Figure 14 Implementation of PM Sagnac Interferometry for detection of acoustic emission signals (The laser source is 2 mW, 830 nm super luminescent diode, SLD)

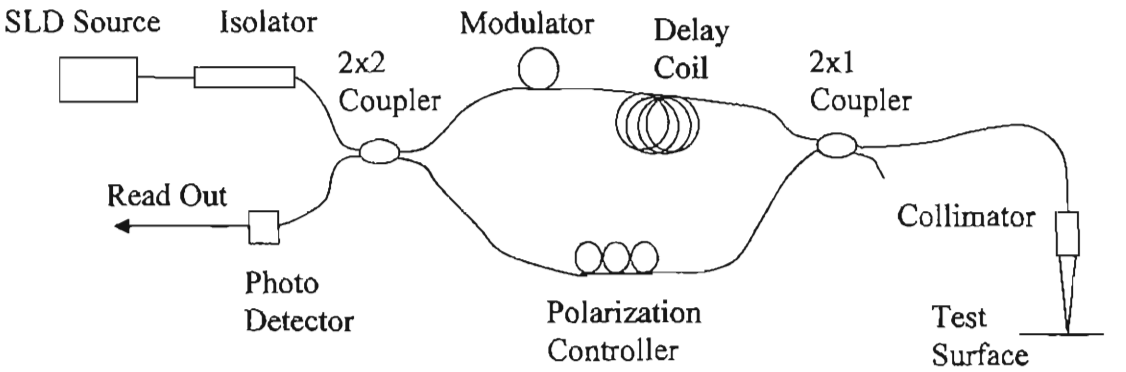

Figure 15 Optical configuration of the economic SAGNAC interferometer

The cost of the PM fiber based device as discussed above is around $10K. A slight variation of the setup, by replacing the PM fiber with SMF 28 single mode fiber, may further reduce the cost of the interferometer to less than $5K. With industrial support, we were able to build an economical version of the SAGNAC interferometer, whose configuration is shown in Figure 15. A photograph of the experimental setup of the SMF 28 fiber system is shown in Figure 16. Figure 17 shows the results of ultrasonic signal detection by using SAGNAC interferometer on a laboratory specimen (smooth aluminum surface). It can be seen that the quality of the signal detected is comparable to those obtained by using TWM (Figure 5a) and MSM PI-EMF (Figure 9a) unit. Unfortunately, none of the SAGNAC interferometers as discussed can produce a reasonable result when used for detecting AE signals from optically rough surfaces, such as rock.

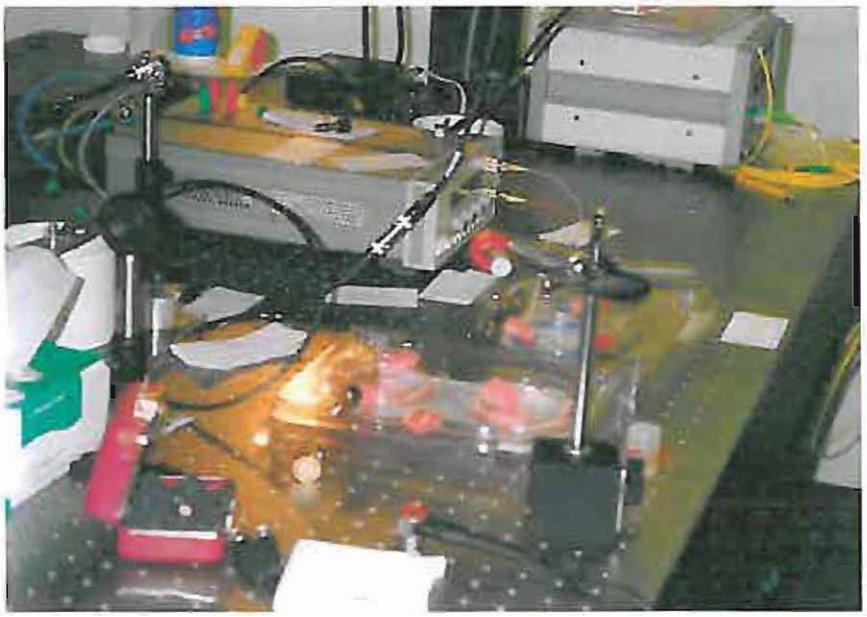

Figure 16 Implementation of Sagnac Interferometry using regular single mode fibers

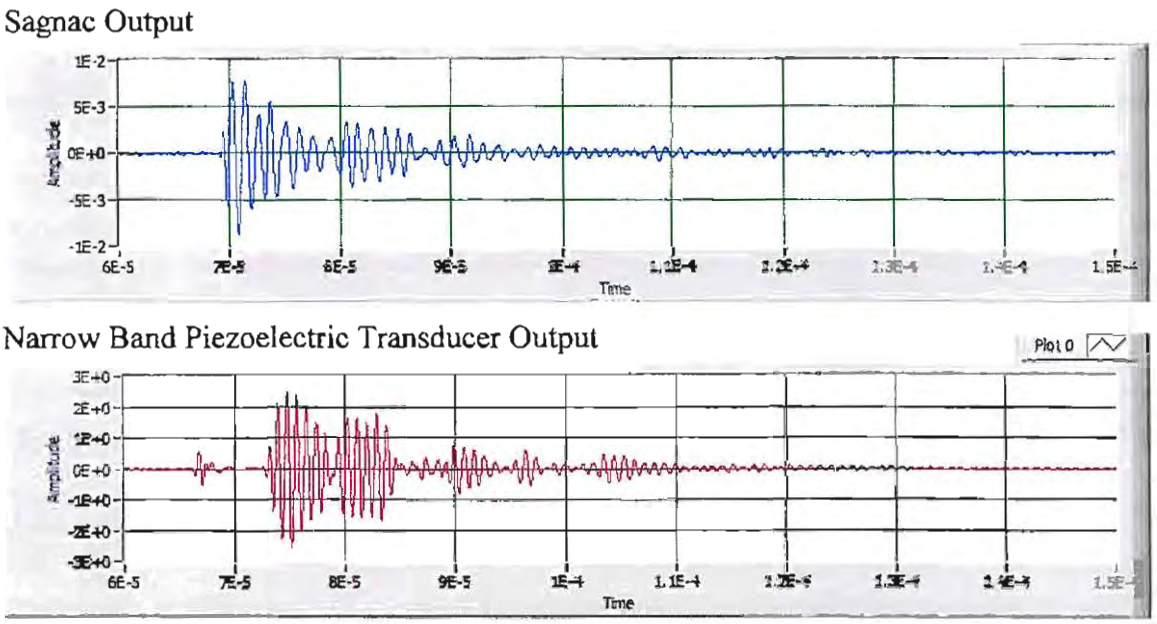

Figure 17 Ultrasonic detection using Sagnac device compared with piezoelectric transducer

3. Sensing unit using TWM device. Trial experiments on the alterative interferometer sensing units (PI-EMF and SAGNAC interferometry), although successful, did not generate a strong candidate to replace TWM device for AE signal detection. The structure of TWM device is relatively cumbersome compared with the other two interferometers tested; however, it provides the best sensitivity and signal to noise ratio, which is very important in the proposed application. Therefore, the remaining effort was focused on development of acoustic emission detection equipment using the TWM device.

The effort in the instrumentation development is to further reduce the dimensions of free-space setup into portable format so that it can be used freely in field applications. Fiberization is a key means to realize device miniaturization. It will not only reduce the size of transmission path, but also eliminate the bulky breadboard required for free-space optics setup. However, several optical functions in TWM device need to be realized in free-space, which result in several free-space to fiber conversions or *vice versa*. Therefore, an effective fiber-launch system becomes crucial for the success of the miniaturization.

A common device for launching laser light into optical fibers basically consists of a lens (lens set), a lens (lens set) holder that is aligned in front of the laser beam, and a means of positioning an optical fiber at the spot focused by the lens. Good launching efficiency relies on optimization of the launching device including lens and positioning mechanism. In selection of lens, one consideration is based on the size of focusing spot:

$$d_{spot} = 2.44 f\lambda / D \qquad \text{(Eq. 4)}$$

where d_{spot} is the diameter of laser beam at focus, f is effective focal length of the lens, λ is the wavelength of laser light and D is the diameter of incident laser beam. For our application the diameter of fiber core is 3.5 μm, the focusing spot should be smaller than this. Given λ is 532 nm and D is approximately 5 mm, the effective focal length of the lens should be <13.48 mm, in order for $d_{spot} < 3.5$ μm. Another consideration is based on the matching of numerical aperture NA or acceptance angle of the fiber:

$$NA = \frac{D}{\sqrt{f^2 + D^2}} \qquad \text{(Eq. 5)}$$

Since the NA for the single mode fiber is 0.12, the effective focal length should be >41 mm to have the entire focused laser beam fall into the acceptance angle. This result is in conflict with the result based on the size of focusing spot, which means for the given single mode fiber, a complete coupling (100% transmission) is not achievable. To find a compromise, three focal lengths (14, 16.5 and 25.4 mm) between 13.48 mm and 41 mm were found and tested. The focal length of 16.5 mm seemed to provide the best result.

In the effort to optimize the fiber positioning mechanism, three fiber-launch devices were obtained: Thorlabs MDE330TH translation stage, Edmund P55-477 fiber alignment mount and OFR PAF-X-5-Vis fiber-port. The setups shown in Figure 18 were used for the transmission efficiency evaluation. So far, the best results of transmission efficiency obtained are 70 – 90% for multimode fiber and 40 – 70% for single mode fibers. The detailed design for prototype TWM instrumentation will be discussed in Section 4.5.

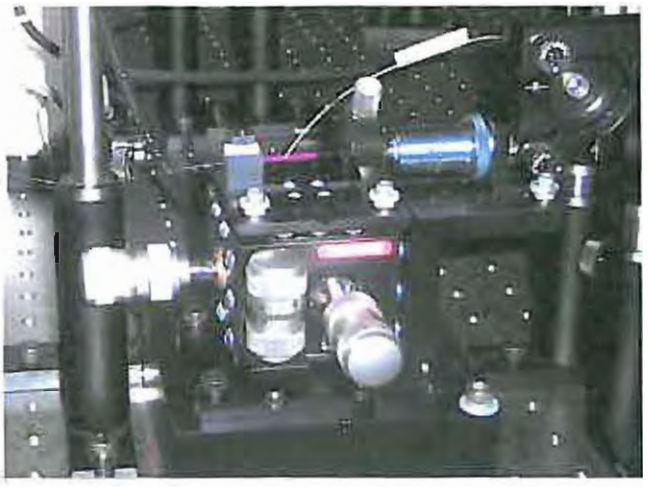

a. Thorlabs XYZ translation stage

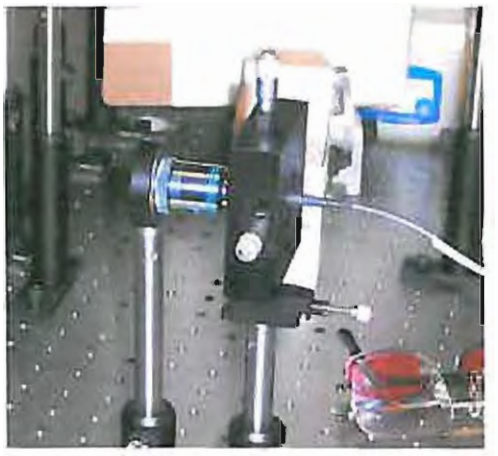

b. Edmund P55-477 ride on Z-translation stage

c. Edmund P55-477 ride on kinematic platform

d. Thorlabs Fiber Coupler

e. OFR Fiberport

Figure 18 Fiber launch devices tested for TWM instrument development

In Sub-Task 1.2, trial experiments on the alternative interferometer sensing units (PI-EMF and SAGNAC interferometry) were conducted. It was found that the performance of the interferometry tested cannot match that of the TWM sensing unit. The fiber launch devices for miniaturization of the TWM sensing unit were also optimized for further instrumentation integration.

4.1.3 Sub-Task 1.3: Digital Audio AE Monitor

Acoustic emission inside a material is an energy conversion phenomenon caused by processes such as inter- or intra-granular friction, or micro fracture development when the material is subjected to external load, as would occur in instability development in mining structures. When the material is approaching failure, more deformation is involved; therefore, more acoustic emission (AE) activities will occur. Figure 19 shows AE signals collected at different loading levels (10%, 60%, and 95% of the ultimate strength) of a rock specimen. By evaluating the behaviors of these AE signals, material failure may be predicted before it occurs. This is the logic of using AE activities for mine stability assessment. Figure 19 demonstrates that

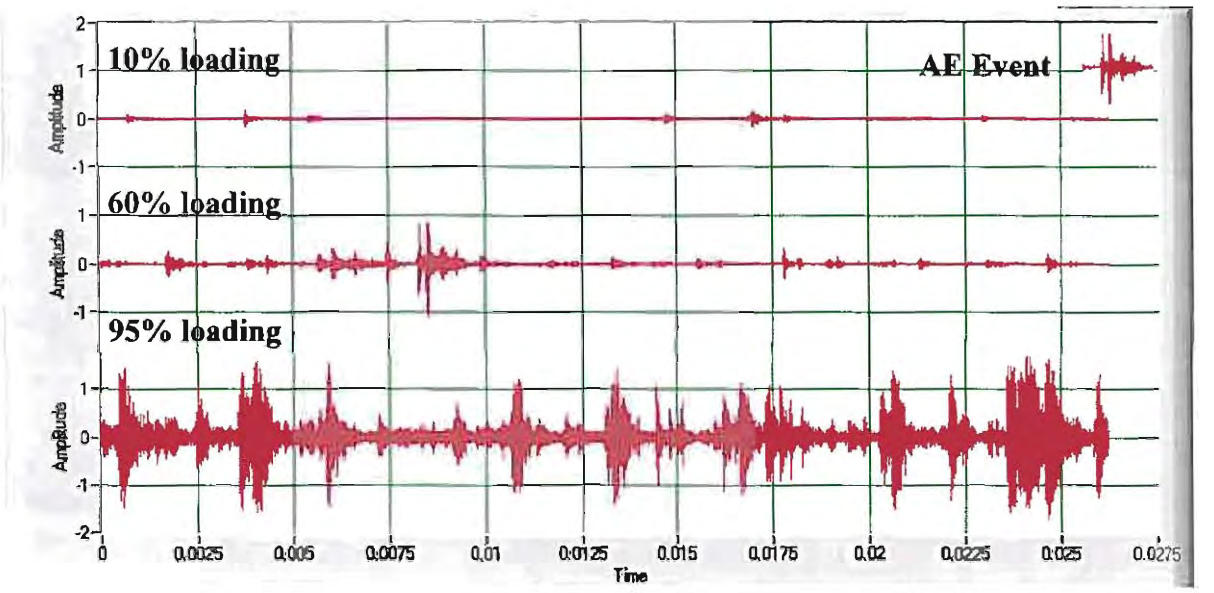

Figure 19 Acoustic emission signals collected at different loading levels

increasing load results in more and more AE events. Both amplitude and frequency of occurrence of the AE activities will increase. It is very intuitive that if these AE events can be heard, the volume and frequency of the occurrence of these AE events may be used to make a very accurate judgment of the stability of the mining structures. Unfortunately, the AE events are more often ultrasonic (50 KHz – 1MHz) and thus inaudible to the human ear. For many years, efforts have been made to convert these ultrasonic signals into meaningful audible sound to help people make judgments on structural stability. A technique, as offered in the original proposal, involves using a heterodyne mixer to generate signals in a beat frequency which is in the audio range. Heterodyne audio AE monitor has been widely used in AE monitoring and warning systems. Experience has shown, however, that it is still very challenging to select a local frequency in order to generate meaningful audible signals (20-20000 Hz) for AE based warning. In this SBIR project, an innovative method of fast-sampling and slow-replay was developed to make the AE signals audible: that is, audible frequency is achieved by stretching the time axis. Toward this goal, 5 MHz sampling frequency is used during AE data acquisition and then the data collected is written into a .wav file using 44 KHz playback rate, which is 113 times slower than the in-situ data. The signal amplitudes remain unchanged. This method translates the AE signals into audible frequency with amplitude and relative frequency of occurrence unchanged. The replay of the sound files (.wav) provides a very good indicator of material instability development.

The digital audio AE monitor takes advantage of the multimedia feature of the CPU processor in the data acquisition and processing function. The software was developed as a part of the software for data acquisition, which is in LabView environment. LabView is based on graphical G-language particularly developed by National Instrument (Austin, TX) for instrumentation use. The audio AE monitor part of the block diagram is listed in Figure 20. Because of its superior performance, the digital audio monitor of acoustic emission, as discussed, has been implemented with the digital data acquisition system to replace the super heterodyne audio monitor in the proposal for real time AE activity monitoring of the prototype instrument. This monitor will prove its significance in later field applications.

Block Diagram

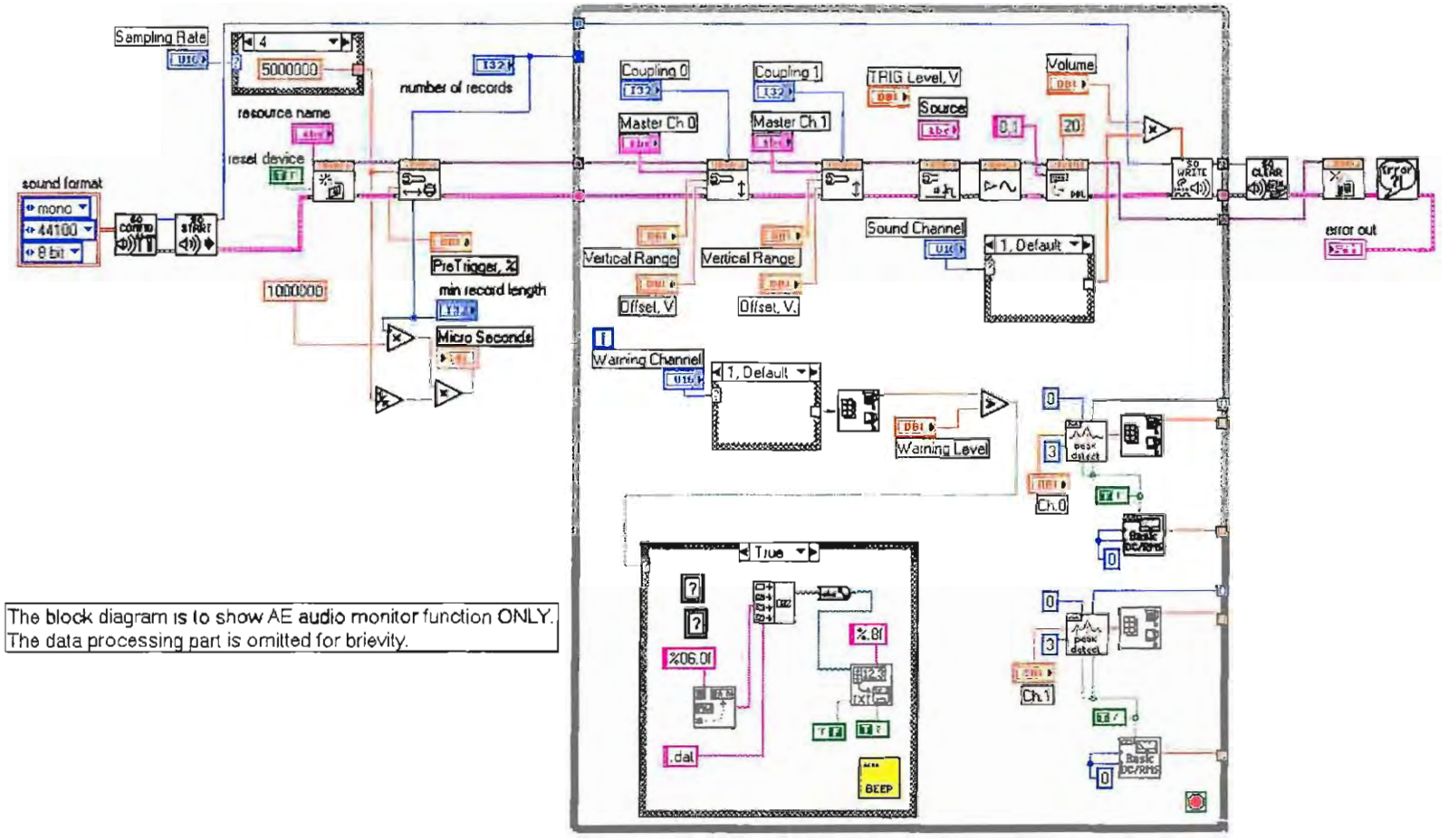

Figure 20 LabView block diagram of digital audio AE monitor for mine instability detection

4.1.4 Rear Earth Doped Fiber Amplifier (Aim 1 Extension)

As discussed in Sections 4.1.1 and 4.2.2, insufficient signal beam intensity is recognized for generating a clear interference pattern at the photorefractive crystal BSO (see Figure 3). This insufficiency may be caused by application of more economical laser source as described in Section 4.1.1, or by low reflectivity of the rock surfaces during the projected field application as illustrated in Section 4.2.2. Therefore, enhancement of laser beam intensity to the required level, approximately 100 dB, becomes a key issue for success of the proposed development. Since the acoustic emission detection is based on optical interferometry, maintenance of phase information of the laser beams is very important. As a result the use of optic fiber amplifier (OFA) is practically the only option. Figure 21a shows a simplified block diagram of ultrasound detection using TWM based sensing unit. It consists of laser source, TWM interferometry and testing surface. There are two possible locations in the TWM based detection that can be used for OFA to enhance the light intensity. One is in front of the interferometry, as shown in Figure 21b, to enhance the laser source illuminating the entire interferometry circuit so that the beam intensity is amplified. TECNAR inc. (Montreal, Canada) used this approach in their laser ultrasonic detection. The laser source is amplified from 200 mW to 500 W (33 dB) to compensate for the low signal beam intensity. The disadvantage of this approach is that a detection beam of high intensity is used, which is extremely harmful to human eyes and difficult to apply in the environment of mining operations. Therefore, the best way in our proposed application is to use the other location as shown in Figure 21c. In this configuration, the OFA is placed on the signal beam. Since the signal beam is amplified both ways, the beam intensity required for AE detection is greatly reduced. Based on this consideration, an OFA will be developed to meet the requirement of signal beam intensity compensation, particularly an optical fiber amplifier with 20 – 30 dB gain working at 532 nm wavelength. Since this requirement was not clearly shown in the previous Phase I study, it is not addressed in the Phase II proposal.

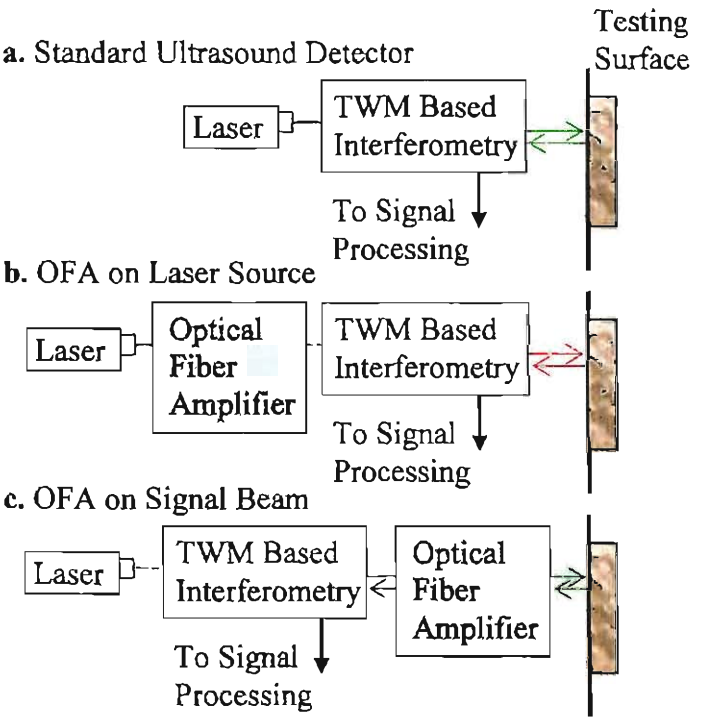

Figure 21 Optical fiber amplifier (OFA) at different locations of TWM based ultrasound detection

Physics. Xie and Gosnell [1995] conducted research on multicolor laser device using Pr^{3+}/Yb^{3+} codoped ZrF_4-BaF_2-LaF_3-AlF_3-NaF (ZBLAN) optical fiber. The fiber was pumped by 780-880 nm wavelength infrared sources and generated green laser tunable in 517-540 nm range. This work provided the experimental foundation for the OFA development.

An energy-level diagram of Pr^{3+} that shows all four visible laser transitions (or amplifier transition) is shown in Figure 22. The level diagram shows that, because the upper laser levels are common to all four laser transitions, the lasers must share the same upconversion pumping mechanism.

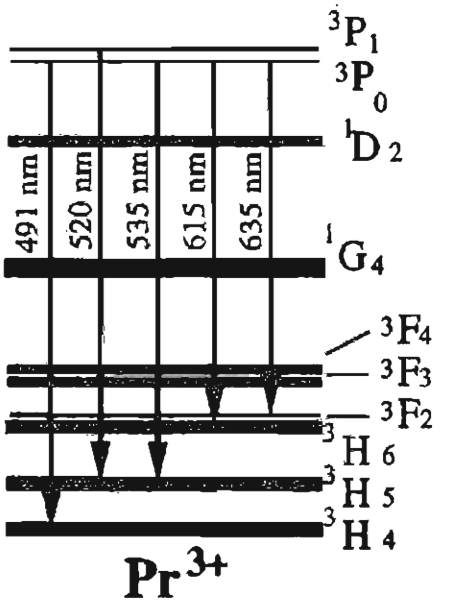

Figure 22 Energy level diagram of Pr^{3+} (after Xie and Gosnell, 1995)

Three upconversion processes have been identified by Xie and Gosnell [1995] to be potentially responsible for the filling of the ^3P upper laser levels. The three processes share one important step: efficient radiationless energy transfer from the optically pumped $^2F_{5/2}$ level of Yb^{3+} to the $^1G_4$ level of Pr^{3+} (see Figure 23). The first possible mechanism simply combines this step with a second radiationless transfer from an optically pumped Yb^{3+} ion, thus promoting the Pr^{3+} ion from the $^1G_4$ level to the ^3P manifold. However, this process was discounted by Xie and Gosnell because it is incompatible with the sharp descent at long wavelengths (>880 nm) of the pump tuning curve – the Yb^{3+} absorption is slowly increasing at these wavelengths and should therefore yield higher, not lower, pump efficiency. This is because the strong central peak of Yb^{3+} absorption in ZBLAN occurs at 975 nm.)

A second and more likely mechanism, one that is compatible with the pump tuning curves, is depicted in Fig. 23a. In this scheme, excited-state absorption of a pump photon on the Pr^{3+} $^1G_4 \rightarrow {}^3P_J$, $^1I_6$ transitions follows the Yb^{3+}-to-Pr^{3+} energy transfer step. Note, however, that Quimby and Zheng [1992] assert that 96% of the oscillator strength in this excited-state absorption step resides in the $^1G_4 \rightarrow {}^1I_6$ transition. A pump process that exploits such excited-state absorption was recommended over the double-energy transfer mechanism by Allain *et al.* [1991], who obtained upconversion-laser output at 635 nm.

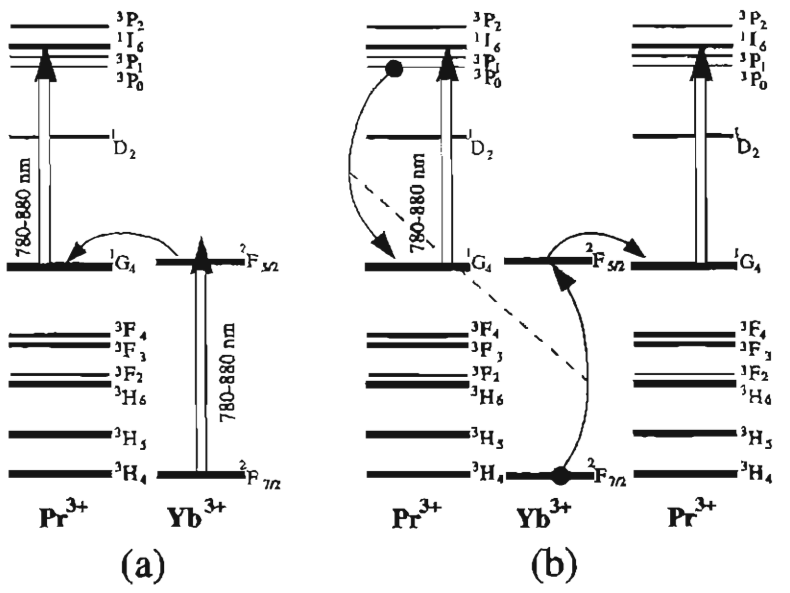

Figure 23 Two upconversion mechanisms for filling the ^3P upper laser level of Pr^{3+} proposed by Xie and Gosnell (1995)

There is a third possible mechanism, one that to our knowledge has yet to be described in the literature, see Figure 23b. In other experiments with Pr^{3+}/Yb^{3+}-doped ZBLAN fiber, Allain *et al.* [1991] identified a

cross-relaxation process between the ^3P manifold of Pr^{3+} and a ground-state Yb^{3+} ion in codoped ZBLAN samples. Significantly, when the ^3P levels are pumped directly at 476 nm, this cross-relaxation process almost completely quenches Pr^{3+} visible emission for an Yb^{3+} concentration of at least 2 wt. %. The result of the cross relaxation is the creation of one Pr^{3+} ion in the $^1G_4$ state and one Yb^{3+} ion in the $^2F_{5/2}$ state. However, efficient transfer from Yb^{3+} to a second $^1G_4$ level – note at this point that there are now two Pr^{3+} ions in the $^1G_4$ level – followed by excited-state absorption within the Pr^{3+} manifold can more than compensate for the single excitation initially sacrificed from the Pr^{3+}–^3P manifold. It is important to recognize that this statement holds true even if the Yb^{3+}-to-Pr^{3+} transfer efficiency is less than unity. The action of the photon-avalanche mechanism just described therefore may account for the extension of the pump tuning range to short wavelengths, a region in which the Yb^{3+} absorption is very weak, and for the relatively short fiber lengths needed for good laser performance. Verifying the efficacy of this pumping process, quantifying its affiliated energy transfer rates, and investigating the role of optical saturation of the excited-state-absorption step offer several avenues for future research that may lead to significant increases in the laser output power. To this end, it is noted that Tropper *et al.* [1994] have already published values for several important parameters relevant to the present results.

Figure 24 shows a visible fluorescence spectrum obtained by collection of side fluorescence from a sample fiber pumped below the lasing threshold. The spectrum thus indicates the relative magnitudes of the laser transition oscillator strengths. The energy concentration between 510 to 540 nm provides an excellent amplification window for development of optical fiber amplifier of 532 nm wavelength using Pr^{3+}/Yb^{3+}-doped ZBLAN fibers.

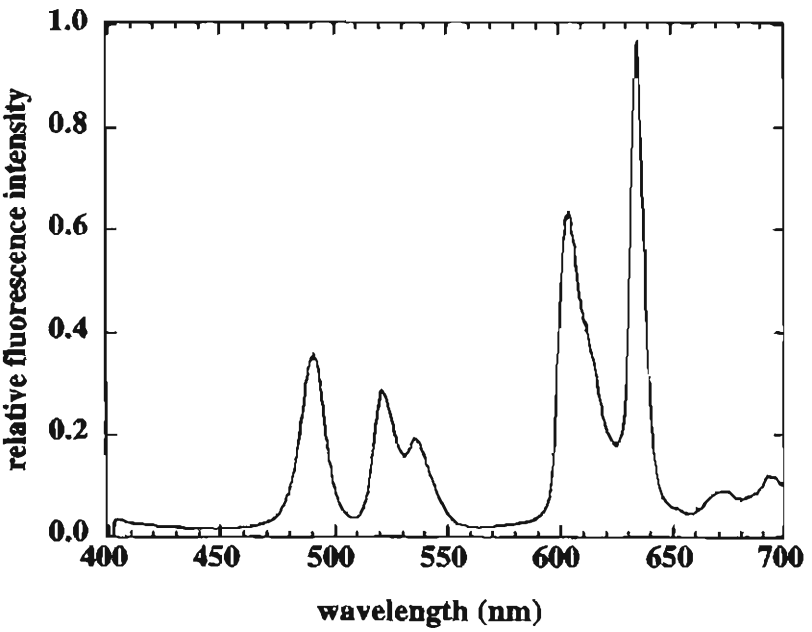

Figure 24 Side-light fluorescence spectrum of Pr^{3+}/Yb^{3+} codoped ZABLAB fiber pumped by 860 nm infrared source (after Xie and Gosnell, 1995)

Design. Optical fiber amplifier was designed and tested for the proposed project use. Pr^{3+}/Yb^{3+}-doped ZBLAN fiber was used for 532 nm unconversion OFA as discussed above. First, multimode fiber was used. The fiber was acquired from *LeVerre Fluore*, France. The multimode fiber has core and cladding diameter of 35 and 125 μm, respectively. The numerical aperture of the MM fiber is 0.3. The ZBLAN fiber was doped with 3000 ppm praseodymium (Pr) and 20000 ppm ytterbium (Yb).

Figure 25 shows the block diagram of the configuration for the optical fiber amplifier using multimode fiber. An 852 nm diode laser is used as pump for the amplifier. First, the 852 nm laser beam is collimated, and passed through a 45° reflective dichroic reflector, then focused by

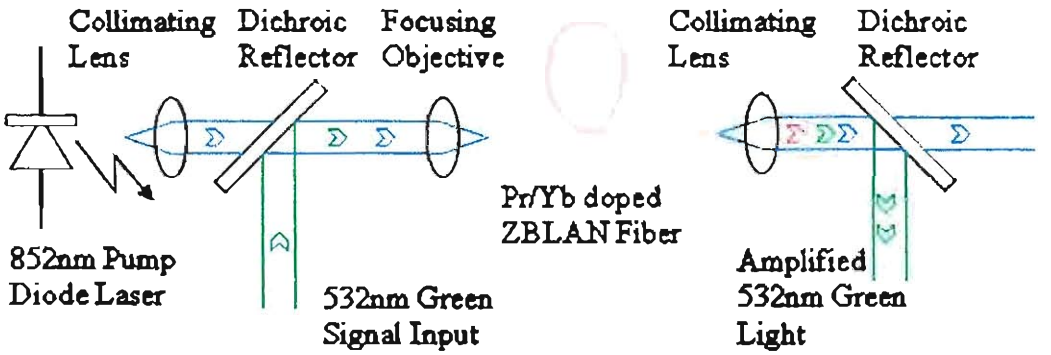

Figure 25 Optical fiber amplifier with one diode laser pump (852 nm)

microscope objective (focusing objective) and launched into the ZBLAN fiber, in order to excite the dopant ions. The pump laser excites the ions into a higher energy level from which they can decay via stimulated emission of a photon at the signal wavelength. Amplification is achieved by the stimulated photon emissions. The signal beam to be amplified is 532 nm green light mingled into the pump beam through the dichroic reflector. The signal beam launched in the ZBLAN fiber provides the excitation to the stimulated photon emissions to create a state of resonance at the same signal frequency so that the intensity of signal beam is enhanced. At the output end of the ZBLAN fiber, the amplified green light is separated from the pump beam after collimation by another dichroic reflector. According to the previous work by Xie and Gosnell [1995], the wavelength of pump laser can be in the 840 to 875 nm range. No exact pump wavelength is necessary. The pump laser selected for multimode fiber was an 852 nm diode lasers in 14-pin butterfly module (B1-852-1500-15A) from Axcel Photonics, Inc., Marlborough, MA. The diode laser has a maximum operating power of 1.5 W and 100-micron 0.22 NA fiber core output with FC end fiber termination. Figure 26 shows the experimental setup of the OFA based on MM ZBLAN fiber.

Figure 26 Photograph of experimental setup of upconversion optical fiber amplifier using multimode Pr^{3+}/Yb^{3+}-doped ZBLAN fiber

A systematic measurement of output power of the optical fiber amplifier was conducted with various input signal levels and pump powers, in order to evaluate the OFA performance. Table 1 shows the results. The results are also plotted in Figure 27. The input power of the signal beam is ranging from 1 μW to 300 μW; and the pump power varies from 0.6 to 1.4 W. As shown by the results, for a given input signal, when pump power increases the output of the OFA increases. This is because more pump power induces more stimulated emission of photons to enhance the signal beam. However, it is also observed that at a fixed pump power, the gain of OFA significantly reduces with the power of input signal. This clearly shows that the gain medium does not reach the state of complete population inversion caused by the insufficient pump power, or in other words, the light intensity is insufficient in the gain medium to excite the Pr^{+3} ions to its ^3P manifold.

Table 1 Output power of MM optical fiber amplifier (unit: μW)

Pump Power W	Signal Power					
	1 μW	10 μW	50 μW	100 μW	200 μW	300 μW
0.6	6.1	15.4	56	107	209	314
0.7	10	19.8	59	114	214	315
0.8	12.8	21	61.5	111	212	310
1	18	28	64	118	213	313
1.2	22.4	31.2	70	127	229	320
1.4	30	41	79	128	229	315

There are two practical ways to increase the light intensity in the gain medium or the ZBLAN fiber. One is to increase the power of the pumping diode laser; the other is to reduce the size of fiber core. To increase the power of pumping diode laser will result in a parallel combination of multiple diode laser units, which is bulky, heavy and inconvenient in field applications. A more reasonable approach would be to use smaller fiber core for the OFA configuration. Therefore further development work was focused on using single mode ZBLAN fiber.

The single mode ZBLAN fiber was also acquired from *LeVerre Fluore*, France. The fiber has core and cladding diameter of 3.5 and 125 μm, respectively. The numerical aperture of the SM fiber is 0.11 and cutoff frequency at 0.5 μm. The fiber was similarly doped with 3000 ppm praseodymium (Pr) and 20000 ppm ytterbium (Yb). The same amplifier structure as shown in Figure 25 was used for the single mode fiber implementation. The diode laser for the setup of single mode fiber is an 852 nm module (M9-852-0150-S50) with 9 mm TO-can package, also from Axcel Photonics. This single mode diode laser has 150 mW maximum operating power. Figure 28 shows a photograph of the optical fiber amplifier with single mode ZBLAN fiber.

First of all, the light intensity in the fiber has been greatly improved. In the case of previous multimode fiber, the core diameter was 35 μm and maximum power transmitted was 748 mW (at 1.5 W pump). The maximum light intensity for multimode fiber during the experiments was 77.7 KW/cm^2. In the single mode fiber setup, the core diameter is 3.5 μm and the maximum transmitted light power was 19 mW (at 150 mW pump), which provide light intensity in the fiber of at least 197.5 KW/cm^2. This indicates approximately a threefold increase of light intensity inside the gain medium, compared with the MM fiber.

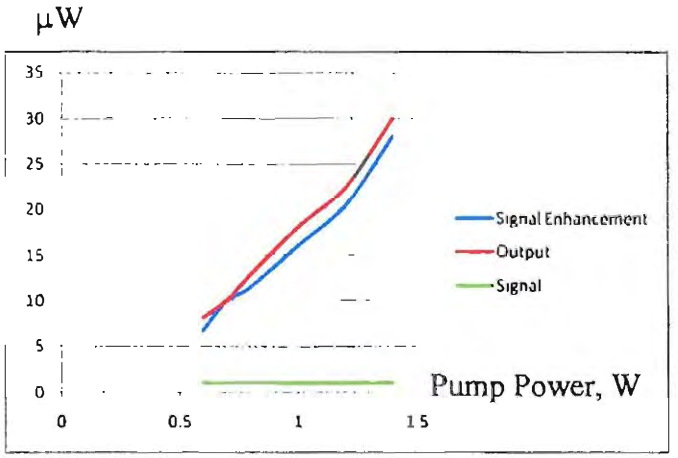

a. Input signal 1 μW

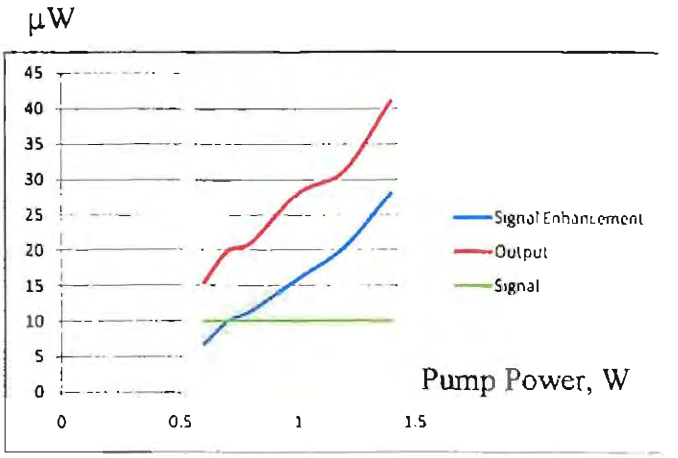

b. Input signal 10 μW

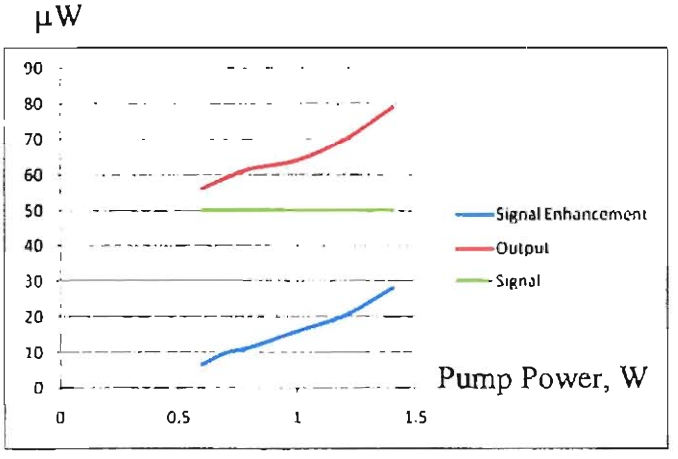

c. Input signal 50 μW

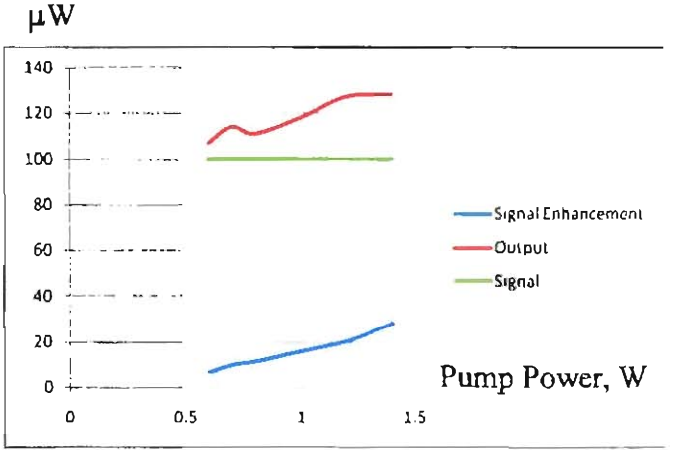

d. Input signal 100 μW

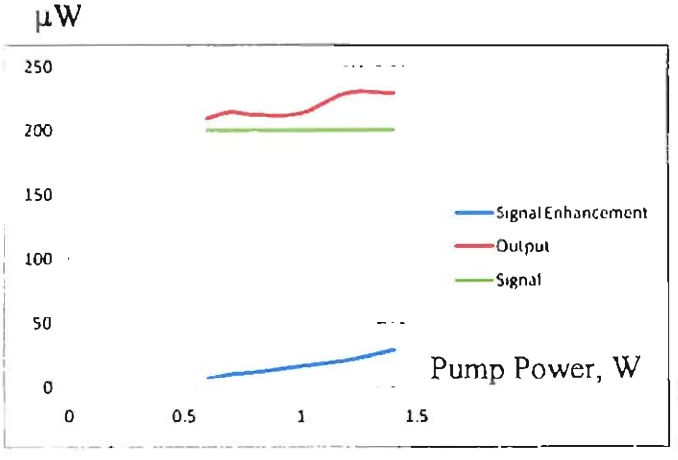

e. Input signal 200 μW

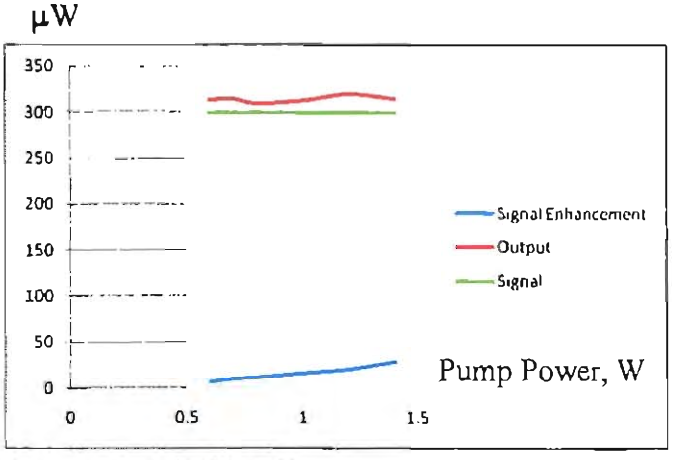

f. Input signal 300 μW

Figure 27 Input – output characteristics of optical fiber amplifier using multimode Pr^{3+}/Yb^{3+}-doped ZBLAN fiber

Figure 28 Photograph of optical fiber amplifier using single mode Pr^{3+}/Yb^{3+}-doped ZBLAN fiber (pump at 852 nm)

Table 2 shows the calibration results of the single mode OFA. It is interesting to note through Table 2 that the effect of amplification by the gain medium becomes more significant. The arithmetic enhancement of input signal power becomes more significant for higher signal levels, compared with the previous MM OFA case; however, the gain of the OFA is still lower at high signal input. This indicates that further increase of the optical light intensity is still necessary to enhance the population inversion in the gain medium.

Table 2 Output power of SM optical fiber amplifier (unit: μW)

Pump Power mW	Signal Power		
	1 μW	10 μW	25 μW
150	4.4	19.8	38.8

Further improvement of the optical fiber amplifier design required more pump power to stimulate photon emissions in the gain medium (ZBLAN fiber). For this purpose, the OFA structure shown in Figure 29 was used. This configuration allows a second pump laser to inject

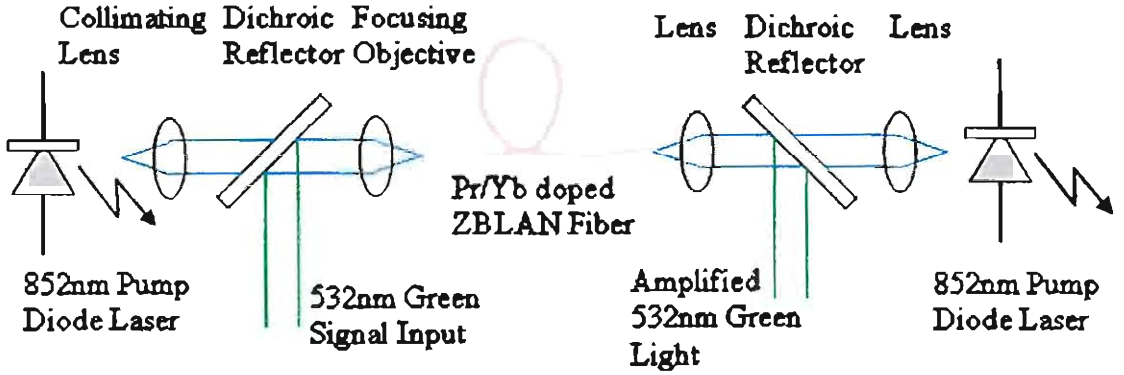

Figure 29 Optical fiber amplifier with two diode laser pumps (852 nm)

pump power from the other end of the ZBLAN fiber, which would double the light intensity in the fiber; meanwhile it will equalize the intensity distribution along the fiber. In this setup, the pump power was increased to a total of 300 mW and the intensity was estimated at 395 KW/cm^2. Figure 30 is a photograph of the OFA setup with two diode laser pumps. On the photo strong fluorescence of the Pr^{3+}/Yb^{3+}-doped ZBLAN fiber can be observed.

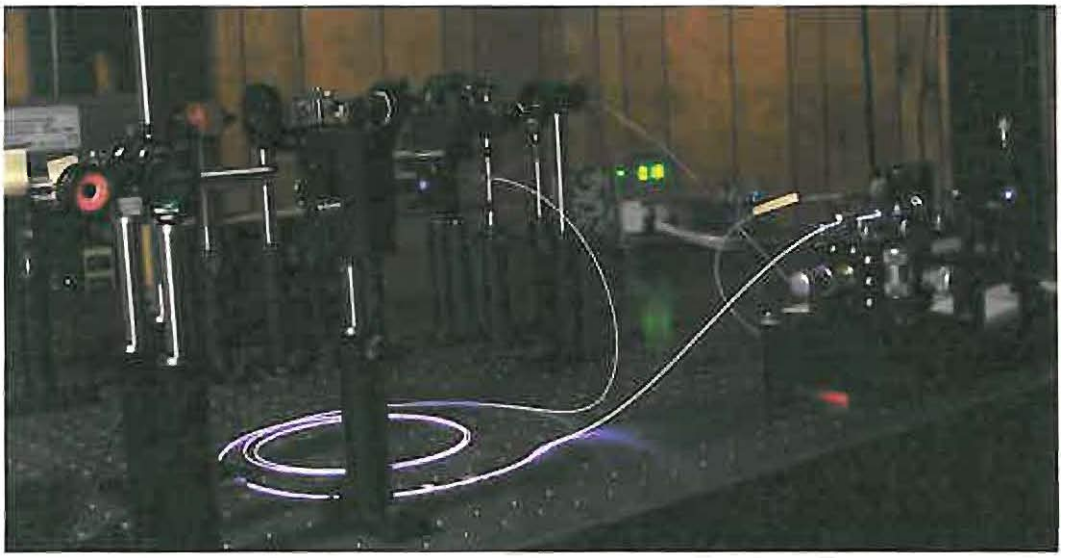

Figure 30 Experimental setup of optical fiber amplifier with two diode laser pumps

Table 3 shows the calibration results of the improved optical fiber amplifier with two diode pumps. It can be observed that at 1 μW signal input the output power underwent slight increase compared with the result of OFA with one pump (see Table 2). Amplification at 10 and 25 μW signal input was significantly enhanced. At 10 μW input, the gain is almost comparable with that of 1 μW input. Thus initial success of the 532 nm optical fiber amplifier has been achieved. The work at this stage is still very primitive. No optimization of the design parameters has ever been carried out. Change of any factors such as fiber length, output coupling, pump wavelength and power may result in variation of the OFA performance. Much work is necessary before the OFA can be implemented in the proposed acoustic emission monitor. Nevertheless, this optical fiber amplifier will be the first 532 nm optical fiber amplifier in the world. At this time, research work on further characterization of this OFA still continues at AAC using private resources.

Table 3 Output power of SM OFA with two pump diode lasers (unit: μW)

Pump Power	Signal Power		
mW	1 μW	10 μW	25 μW
300	6.1	55.8	108.5

4.2 Aim 2: Pre-Field Experiment Preparation

Before the field data collection, preparation will be carried out in the laboratory to evaluate the laser-based instrumentation developed from Aim 1 work, particularly to characterize the behaviors of the instrumentation by collecting acoustic emission data from rock materials extracted from the mining field. Pre-field experiment preparation for in-situ data collection with the instrumentation developed in Aim 1 involves two sub-tasks:

Sub-Task 2.1 Rock specimen preparation
Sub-Task 2.2 Trial AE signal collection using the improved laser device

4.2.1 Sub-Task 2.1: Rock Specimen Preparation

A limited number of rock specimens (6) were prepared for testing surface optical reflectivity. This was to help provide parameters for optical instrumentation development. The specimens used in the tests were selected from the surplus rock materials obtained for the previous Phase I project. Rock specimens with diameter of 2 in. and length of 4 in. were acquired from a potential test mine site for field experiments (Hazleton Pit, Pennsylvania). The detailed geological and site information of the mine site are given in the Phase I final report [Sun et al., 2005]. Rock materials from both coal seam and surrounding bedrock were used, including sandstone, coal and shale. The unfinished rock core surfaces were used for optical reflectivity tests.

Since the major effort of the project has been focused on instrumentation development and preparation of AE signal simulation and recognition, as described in Section 4.1, 4.4 and 4.5, the selection of test mine sites has not been finalized although several mining facilities were identified as potential candidates. After the test mine sites are finally selected, more rock specimens will be obtained for mechanical property evaluation.

4.2.2 Sub-Task 2.2: Trial AE Signal Collection Using the Improved Laser Device

The trial tests in preparation for field experiment at this program stage involve evaluation of surface reflectivity of various rock materials, including sandstone, coal and shale, for laser source selection in the instrumentation development. In the previous Phase I study, significant reduction of light intensity was observed during AE detection on sandstone surface [Sun et al, 2005]. It is necessary to quantify the loss of light intensity so that suitable compensation can be designed. For this purpose, the reflectivity of rock surfaces is evaluated. The setup for reflectivity evaluation is shown in Figure 31. The incident light is reflected by a polarizing beam splitter (PBS) and projected onto the rock surface through a quarter wave plate and focusing lens. The reflected light from the rock surface will pass though the focusing lens (for collimation), quarter wave plate and PBS for intensity measurement. The quarter wave plate serves to control the polarization of the reflected beam so that it can make a straight passage through the PBS. Figure 32 shows a photograph of the experimental setup for

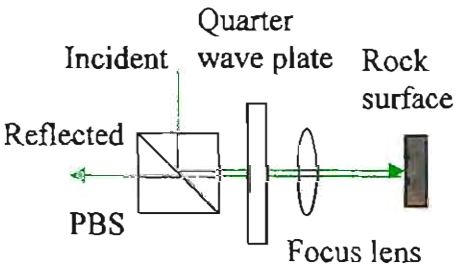

Figure 31 Setup for rock surface reflectivity evaluation

Table 4 Reflectivity evaluation of rock surfaces

Material Surfaces	Incident Light (mW)		Reflectivity	Loss (dB)
	260	115		
Mirror	248	109	0.95	0.2
Aluminum (unpolished)	83	23	0.2 – 0.32	4.9 – 7
Sandstone	1.5	0.56	0.0049 – 0.0058	22.4 – 23.1
Shale	1.1	0.75	0.0042 – 0.0065	21.9 – 23.8
Coal	2.3	1.0	0.0087 – 0.0088	20.6

reflectivity evaluation. The measurement results are listed in Table 4. It can be seen that there is a surface reflection loss of approximately 20 dB from the rock surfaces. For unpolished aluminum surface, where the TWM sensing unit works well, the loss of surface reflection is only 4.9 – 7 dB. Therefore in order to obtain good AE detection on rock surfaces, a minimum of 15 dB intensity compensation will be necessary for the signal beam. Further discussion on signal beam intensity compensation is provided in Section 4.1.4.

Figure 32 Surface reflectivity evaluation of rock materials (532 nm wavelength)

4.3 Aim 3: In-Situ Data Collection

The work planned for Aim 3 is to collect in-situ acoustic emission data from various mining structures in selected mines for further AI function development. Since instrumentation development is still underway at this time, no activity has been carried out for Aim 3.

4.4 Aim 4: AI Criteria Development

The work in Aim 4 is to build criteria for instability development inside the rock structures based on the acoustic emission waveforms collected from the mining sites. Finite element model (FEM) will be used to describe stress conditions (or instability development) and to simulate acoustic emission activities inside mining structures for criteria development. Two sub-tasks are involved in this effort:

Sub-Task 4.1 FEM analysis on underground testing structures
Sub-Task 4.2 AE waveform feature classification

Criteria for instability development, or failure criteria, of materials have been a research topic in classical mechanics for more than two centuries. Many theories have been developed and used in the engineering field. The most popular of these are: Coulomb's theory based on maximum principal stress, Tresca's theory based on maximum shear stress, Mohr and Coulomb's theory based on Mohr's circle, and Griffith's theory based on fracture development. All have advantages and drawbacks in their applications. The references of these failure theories may be found in Jaeger and Cook [1969], Müller [1974], and Jumikis [1983].

In this proposed research work, Coulomb's maximum stress theory is used in the instability criteria development because of its simplicity and intuition. The maximum stress criterion states that failure occurs when the maximum principal stress reaches the ultimate strength of the material. Thus, the percentage of maximum stress in relation to the ultimate strength provides a convenient measurement of the instability development of rock structures, such as 10%, 20%, ... 80%, 90%, etc., indicating how close the instability development is to the failure point. Here, maximum compressive stress is used as primary indicator as conventional in rock mechanics study, and maximum tensile stress and maximum shear stress (Tresca's theory) are used as references. Therefore, the AI criteria development for instability in rock structures involves two steps: first, find maximum compressive (tensile, shear) stresses, or stress levels, at various stages of the mining structure's life cycle; second, extract features of the AE signals collected at the corresponding stress levels in Aim 3. A one-to-one correspondence is then established between the stress levels inside the rock structure and the AE signal characteristics. These extracted features will be used as AI criteria to identify the AE signal detected, in order to determine the stress level or the degree of instability development inside the rock structures through their one-to-one correspondence.

4.4.1 Sub-Task 4.1 FEM analysis on underground testing structures

Finite element analysis has been under development for more than half a century. Since the rapid decline in the cost of computers and dramatic increase in computing power, finite element model (FEM) has now been developed to an incredible degree of precision and speed.

In order to find locations where the AE signals are collected or to locate a monitoring spot where the mining structure is in critical stress state, FEM will be used to simulate the underground mining structures to find stress distribution under the in-situ conditions during various stages of their operating life cycle. It will then be used to locate the points of maximum stresses, including maximum compressive stress, maximum tensile stress, and maximum shear stress inside the mining structures, as well as their values. These stress values will be used as indicators for instability development for AE monitoring station location as discussed above.

Model. Figure 33 shows a layout of a popular longwall mining structure in US coal mines, which complies with 30 CFR 75 regulations. This is a typical longwall mining stope surrounded by panel entries of development, head and tail entries. Preliminary finite element models of the mining structure are based on this layout, which can be easily modified to simulate an actual mine site for field experimentation. FEM models for three basic mining structures were constructed for the subsequent field experiments, namely: entry panel, longwall face and tail (head) gate. Because at this stage the selection of mine sites for actual field trials has not been finalized, the geologic parameters of a candidate mine were used for the model development. To obtain optimal results in numerical simulation of failure criteria development, all FEM simulations will use 3-D models. ABAQUS CAE was used in the FEM model construction. ABAQUS CAE is a software package for finite element modeling. Users can work in a graphical interactive environment to create and modify geometry, import models for meshing, or integrate geometry-based meshes. Figures 34 and 35 are plots of the preliminary FEM models built to support the field experiment and acoustic emission study for instability criteria development.

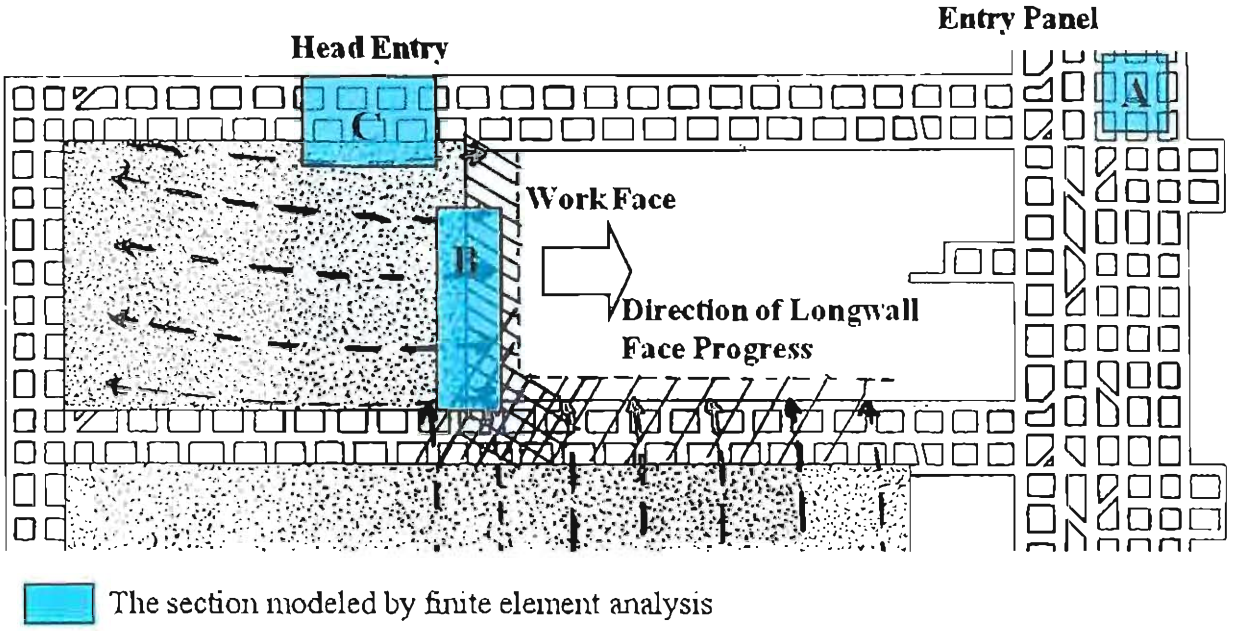

Figure 33 Typical longwall mining structure for FEM model development in preparation of AE signal characterization

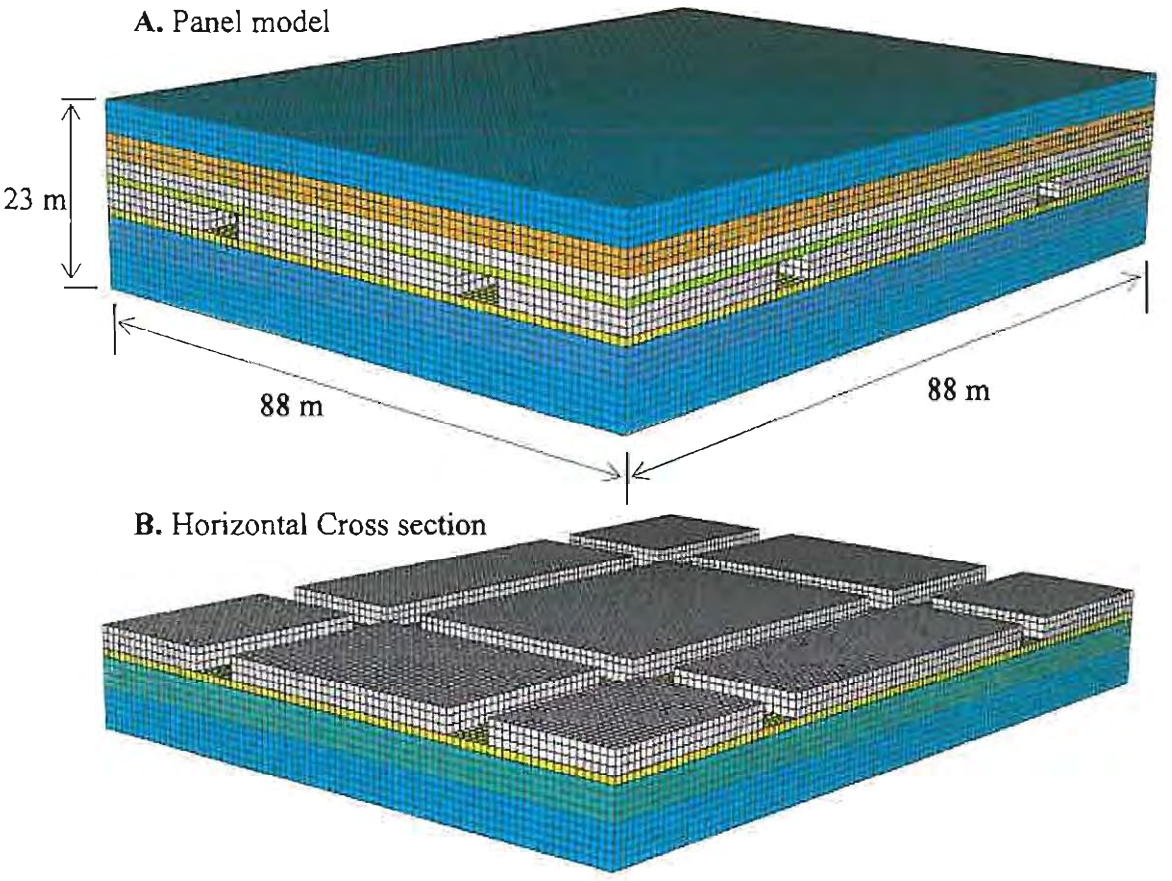

Figure 34 Finite element model of typical coal mine panel

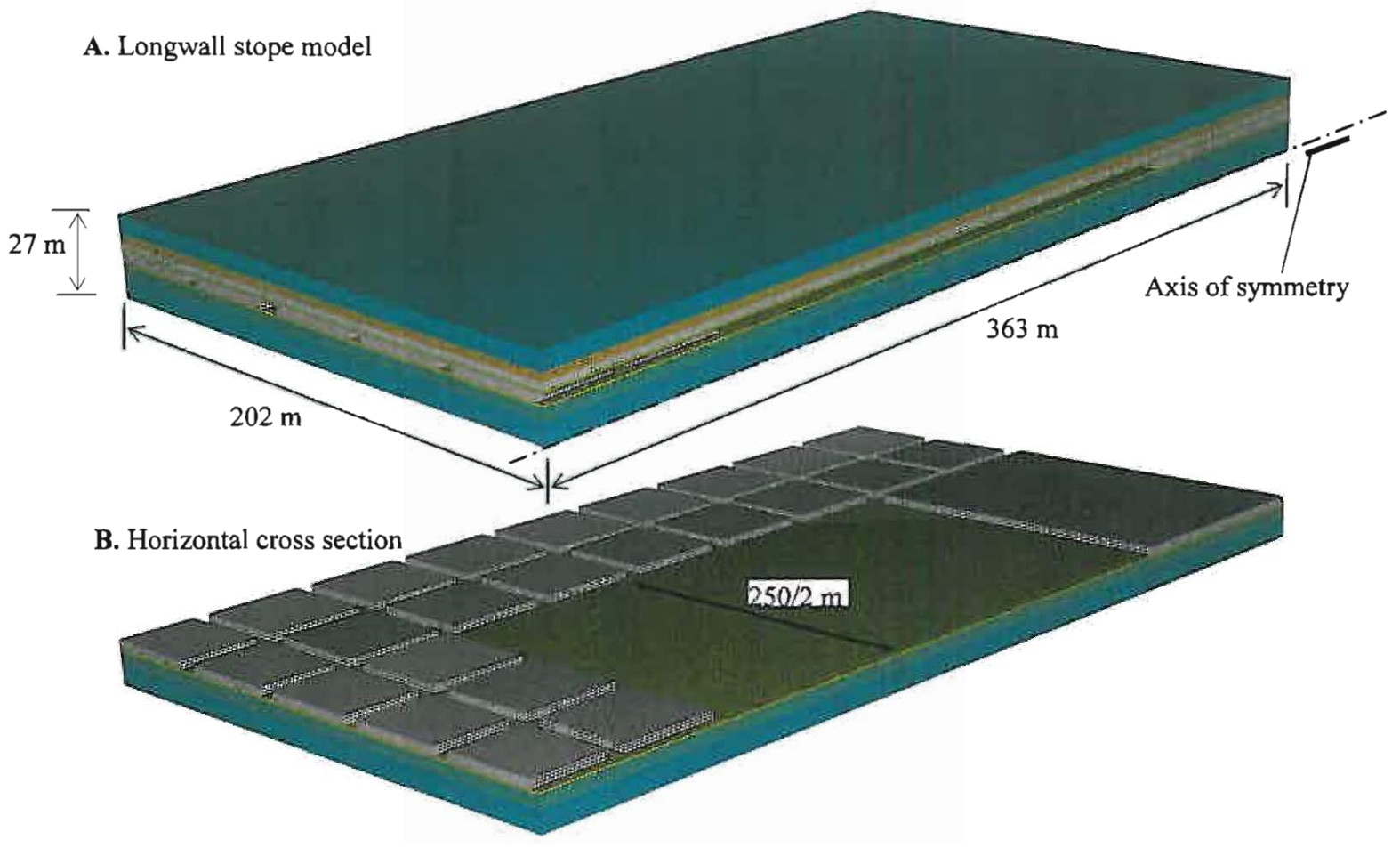

Figure 35 Finite element model of typical longwall stope simulation (symmetrical model)

Node. Nodes are the points where the elements are connected. Nodal points are the locations for displacement calculation of the model. For a given model geometry, a large number of nodes will provide detailed description of stress/strain distribution. However, the amount of computing time will also increase accordingly. There must be a balance between the requirement of accuracy for stress/strain description, and economy of computer (FEM) simulation (CPU time). In this current FEM model, acoustic emission simulation will be conducted to provide input for the proposed AE signal characterization. Consideration must also be given to the accuracy of simulated AE waveforms. Past research in mining structures showed that the frequency contents of AE signals from field study usually span from tens to a little over one thousand Hertz [Hardy, 2003]. If 1500 Hz is used as the upper limit of the frequency contents, given the average acoustic velocity of 3000 m/s in rock mass, the wavelength λ will be 2 meters. According to Nyquist theorem, there have to be at least two nodes along each wavelength in the model. That is to say, the nodal distance has to be less than 1 meter. In actual field measurement, the majority of the AE signals fall in the 100 – 500 Hz frequency band. One meter nodal distance will provide 6 – 30 nodal points along each wavelength, which is considered sufficient for AE signal analysis. Therefore one meter nodal distance was selected for the FEM model. This nodal distance will also suffice in stress/strain distribution description in static analysis.

Element. Because the mining structures simulated are regular in shape, hexahedral (brick) elements (C3D8R) were used for the entire model. The element uses reduced integration to form stiffness matrix, which reduces running time. This is very important in 3-D simulations. The element also has hourglassing effect control to avoid unnecessary distortion caused by reduction of integration point. Based on the above discussion of nodal distance, the element was 1 cubic meter brick. The element mesh is automatically generated by ABAQUS CAE software.

Material. Since the selection of a testing mine site has not been finalized at this time, the material parameters used for the preliminary model are obtained from a potential candidate mine. The parameters present very typical properties of the rock strata surrounding coal mines in the eastern US. There are eight layers of different rock materials from top to bottom of the model, as shown in Table 5. Although rock materials are inhomogeneous and anisotropic, linear elastic material properties have been proven to provide a reasonable approach in much past research. In the later research work, we will also consider using linear poro-elastic materials for the model to

Table 5 Mechanical properties of rock strata

Material	Young's Modulus, E (GPa)	Poisson's Ratio, υ	Density, γ (Kg/m^3)	Thickness, h (m)
Medium grain sandstone	10	0.2	2600	4~6
Fine sandstone and mudstone	6	0.25	1900	3
Coarse sandstone and shale	3	0.2	2000	2
Top coal	3.5	0.3	1500	1
coal	3.5	0.3	1346	3
mudstone	8	0.25	2200	1
Coarse sandstone	12.5	0.2	2400	4
Medium grain sandstone	10	0.2	2600	5~7

The rock strata are listed from top of the model down sequentially.

account for the influence of porosity and fluid flow of the rock mass. The material parameters listed in Table 5 involve Young's modulus, Poisson's ratio, and bulk density used for the simulation. The actual values of these parameters need to be refined in further research work by back analysis from the field measurement and testing results.

Boundary Conditions (Constraints). On the model of coal mine panel as shown in Figure 34, slider hinges are used for all nodal points at the bottom to support the force in the vertical (z-) direction; only one fixed hinge is used at one bottom corner to keep the model from sliding horizontally. On the two end faces of the model perpendicular to the panel axis, displacement is fixed to zero in the normal direction to simulate a plane strain situation.

On the longwall stope model in Figure 35, the same constraints are applied to the bottom as in the coal mine panel model in Figure 34. Since this is a model of one half of the mining stope, displacement and rotation are fixed to zero on the plane of symmetry in order to realize symmetric simplification.

Load. Three different loads are applied to the FEM models to simulate the real loading conditions of the mining structures, namely: the pressure of overburden, lateral pressure on the sides, and body force (gravity) of the mining structure. The overburden pressure on top of the FEM models is calculated based on the gravity of overburden as:

$$p_{burden} = g \sum_{n} \gamma_n h_n \qquad n = 1,2,\ldots \qquad \text{(Eq. 6)}$$

where p_{burden} is the pressure caused by overburden strata, g is gravitational acceleration, γ_n and h_n are the density and thickness of the nth rock layer, respectively. In the preliminary models, we used one layer overburden with average rock density of 2600 kg/m^3. The depth of overburden is 100 m. The value of p_{burden} calculated is 2.548 MPa applied on the top surface of the FEM models. The lateral pressure on the FEM model is caused by the lateral pressure of overburden material, since no tectonic pressure is considered in this case. The lateral pressure is calculated by using the following expression:

$$p_{lateral} = \frac{\mu_n}{1-\mu_n} g \sum_{n} \gamma_n h_n \qquad n = 1,2,\ldots \qquad \text{(Eq. 7)}$$

in which μ_n is Poisson's ratio of the stratum where lateral pressure is calculated. Table 6 lists the lateral pressures on each of the rock layers in the FEM model, calculated through Equation 7. Strictly speaking, lateral pressure is a variable even in the same rock layer, and it increases linearly with depth. For simplification, we used the lateral pressure at the midpoint of each rock layer as uniform lateral pressure applied to that layer. Finally, the body force of the mining structure is caused by gravity,

Table 6 Lateral pressure calculated for each rock layer in the FEM model

Rock Layer	Lateral Pressure MPa
Medium grain sandstone	0.6561
Fine sandstone and mudstone	9.0296
Coarse sandstone and shale	0.6941
Top coal	1.2014
coal	1.2130
mudstone	0.9537
Coarse sandstone	0.7297
Medium grain sandstone	0.7638

$g\gamma_n$. Body force is a distributed load. ABAQUS CAE has an internal function to integrate and distribute the force to each node based on the density of the material and size and shape of the element used in the FEM model.

Static analysis on the FEM models, using ABAQUS/Standard software, generated stress distribution descriptions of mining structures as shown in Figure 36 and 37. Figure 36 describes Mises stress, σ_{mises}, distribution around the mine pillar in the development panel. Figure 37 shows the distribution of maximum compressive stress (or minimum principal stress in classical mechanics) around the longwall stope. High stress concentration at the corners (pillar), sidewalls and working face indicated that these places are prone to fail and generate acoustic emission activities in the mining life cycle. These stress distribution plots provide guidance on where the acoustic emission monitoring should be conducted for safety evaluation. Based on these observations, three locations were selected for FEM simulation of AE activities in longwall mining structure, in order to provide input for AE signal characterization. These selected locations are blue-marked in Figure 33.

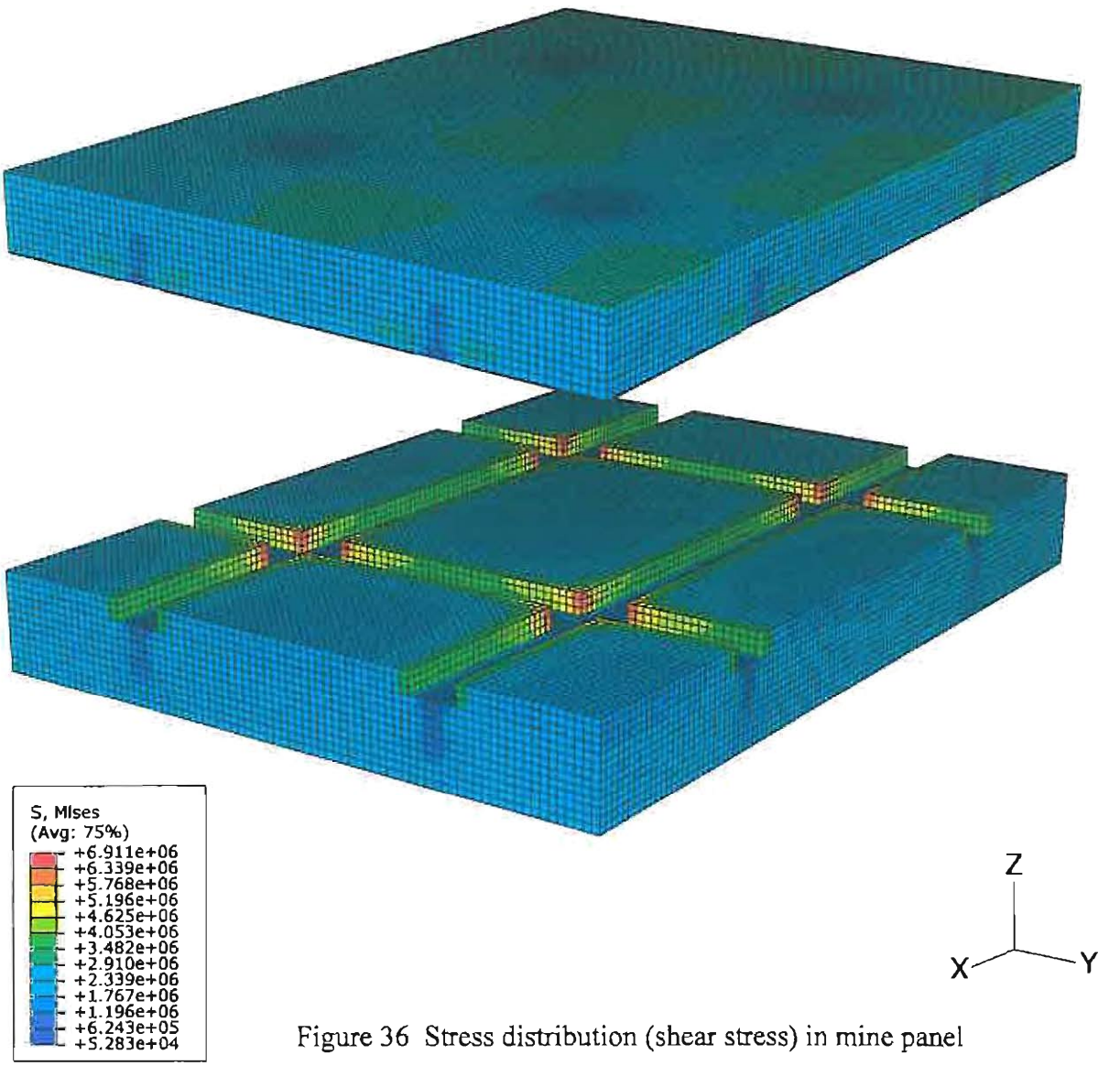

Figure 36 Stress distribution (shear stress) in mine panel

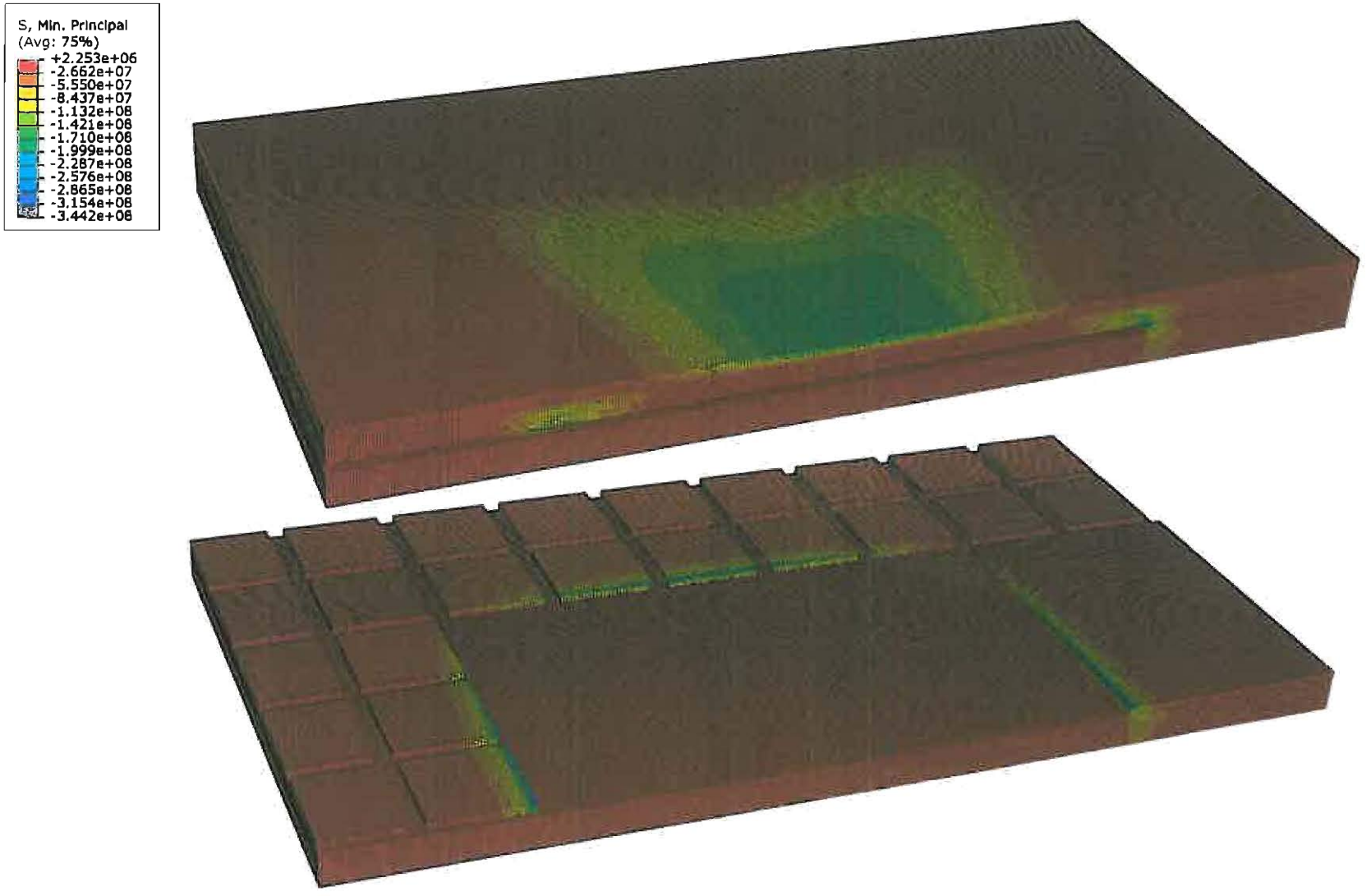

Figure 37 Stress distribution (max. compressive stress) around longwall stope

FEM Simulation of AE Activity in Mining Structures. In classical fracture mechanics, three basic modes of fractures are defined as Type I, II and III, corresponding to opening, shearing and tearing movement of the crack surfaces as shown in Figure 38. Researchers have suggested that these fractures are created due to a dipole of forces acting on the potential crack surfaces as shown in the figure [Dahlen and Tromp, 1998]. When the magnitude of the dipole reaches a certain value, the material sustaining the load of the dipole fails locally, creating fracture inside the material, which is accompanied by energy release in the form of heat or sound, or both. The stress field around the fracture will then be redistributed. Considering Type I fracture, we assume the stress, σ_n, normal to the fracture plane before the fracture development sustains the action of dipole, the following relation holds:

$$F = 2\sigma_n ad \qquad \text{(Eq. 8)}$$

where F is the magnitude of the dipole, a is half crack length and d is the thickness of the material. At the instance of fracture formation, the dipole suddenly loses the support. It becomes two forces with the same magnitude F acting respectively on the two opposite surfaces of the fracture developed. Since the duration of fracture development is very short, it can be considered as two δ-functions with amplitude F acting respectively on the two opposite surfaces of the fracture, which create a source of acoustic emission in the material. Similar discussion for Type II and III fractures will lead to the δ-functions for acoustic emission sources in shear- and tear-fracturing processes with:

$$T = 2\tau_n ad \qquad \text{(Eq. 9)}$$

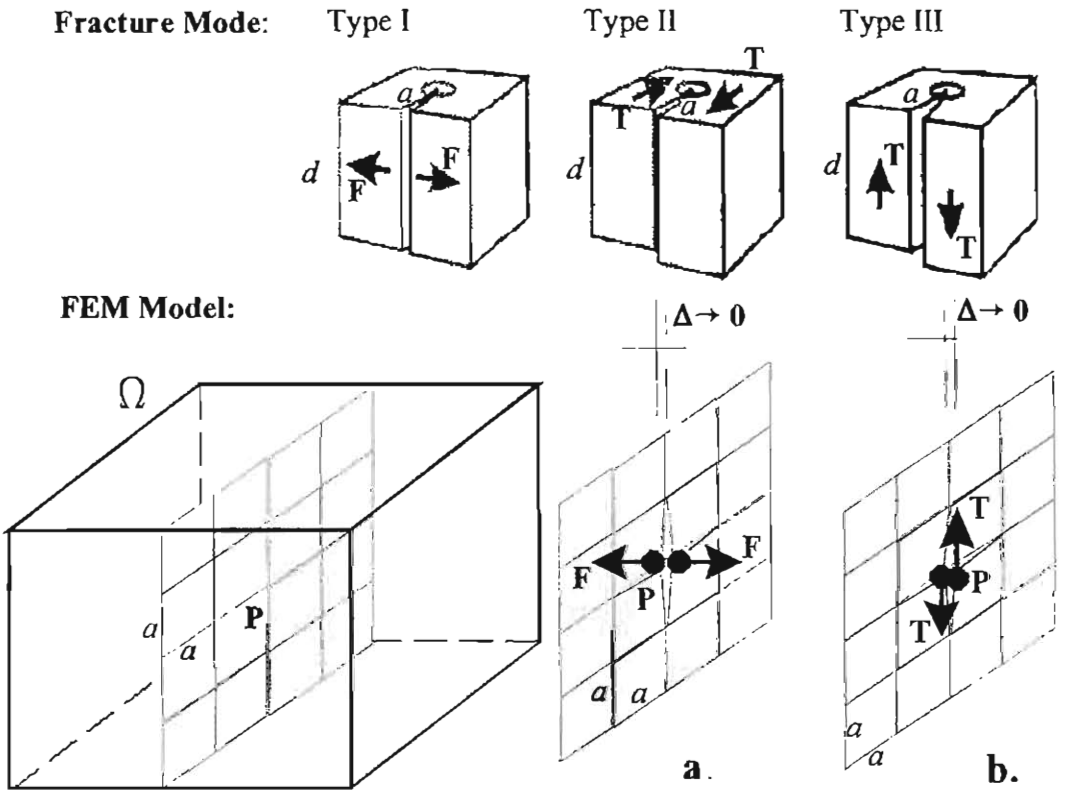

Figure 38 FEM simulation of acoustic emission generation by fracture initiation

where T is the magnitude of the δ-functions parallel to the fracture surfaces, *a* is half crack length and *d* is the thickness of the material, and τ_n is shear stress on potential fracture plane.

As discussed above, the acoustic emission source can be realized by FEM simulation. Figure 38 also shows a FEM model Ω consisting of hexahedral (cubic) elements with dimension of half crack length, *a*. The blue colored cross section shows the interface between two parts of the element assembly, in which fracture development will occur. Suppose the fracture will break the bonds of four elements in the middle of the interface. The acoustic emission sources can be simulated by δ-functions, F for Type I fracture as shown in Figure 38a and T for Type II and III fractures as shown in Figure 38b. In the FEM simulation, the element assembly Ω has to be disengaged at node P on the interface as shown in Figure 38a and b, respectively, to simulate fracture development. Since the size and shape of the element can vary based on the requirement of the simulation problem, FEM simulation of AE activity provides reasonably good flexibility for a variety of AE sources. Johnson [1987] used this concept in his AE simulation in a 2-D problem and obtained results very closely matched to the experimental outcome and the results from other simulation methods (Green Functions).

In 3-D FEM simulation of acoustic emission using cubic elements in our current problem, the magnitudes of δ-functions become:

$$F = 4\sigma_n a^2 \quad and \quad T = 4\tau_n a^2 \qquad \text{(Eq. 10)}$$

where F is the magnitude of δ-functions for Type I fracture and T is that for Type II and III fractures. *a* is the dimension of side of the elements in the model. σ_n and τ_n are stresses on the fracture surfaces which can be found conveniently through static analysis. The TIE function in ABAQUS CAE software provides the capability to connect/disconnect bonds between elements across the interface of the element assembly. Figure 39 shows the locations of simulated AE sources on the selected mining structures (a. mine panel, b. sidewall, and c. working face) for FEM modeling. Two monitoring stations or output locations of AE activity were selected on the model for each mining structure to provide comparison of AE signals detected at different locations as shown in Figure 39.

Simulation Algorithm. ABAQUS supports two dynamic integration algorithms for wave propagation simulation, which are broadly characterized as implicit and explicit. The calculator ABAQUS/Standard supports the implicit method, while ABAQUS/Explicit supports the explicit method. Since the ABAQUS/explicit calculator does not support poro-elastic material as planned for use in further study, the use of the implicit method in ABAQUS/Standard was selected. The implicit algorithm used for time integration of dynamic problem is defined by the following:

$$M^{NM}\ddot{u}^M\big|_{t+\Delta t} + (1+\alpha)(I^N\big|_{t+\Delta t} - P^N\big|_{t+\Delta t}) - \alpha(I^N\big|_t - P^N\big|_t) + L^N\big|_{t+\Delta t} = 0 \qquad \text{(Eq. 10)}$$

where $u\big|_{t+\Delta t} = u\big|_t + \Delta t\dot{u}\big|_t + \Delta t^2[(\frac{1}{2}-\beta)\ddot{u}\big|_t + \beta\ddot{u}\big|_{t+\Delta t}]$,

and $\dot{u}\big|_{t+\Delta t} = \dot{u}\big|_t + \Delta t[(1-\gamma)\ddot{u}\big|_t + \gamma\ddot{u}\big|_{t+\Delta t}]$, with $\beta = \frac{1}{4}(1-\alpha)^2, \gamma = \frac{1}{2} - \alpha, and -\frac{1}{3} \le \alpha \le 0.$

a. Horizontal Cross Section of Mine Panel

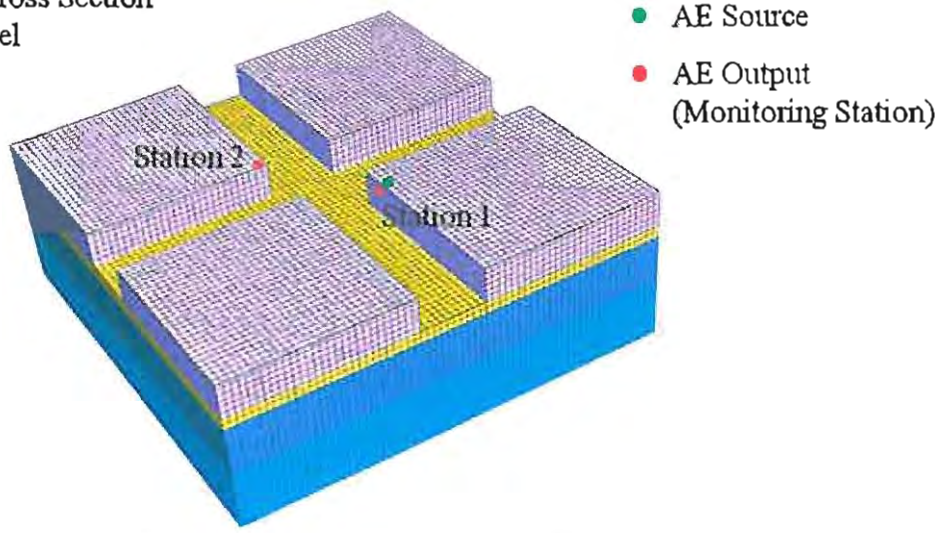

b. Horizontal Cross Section of Sidewall

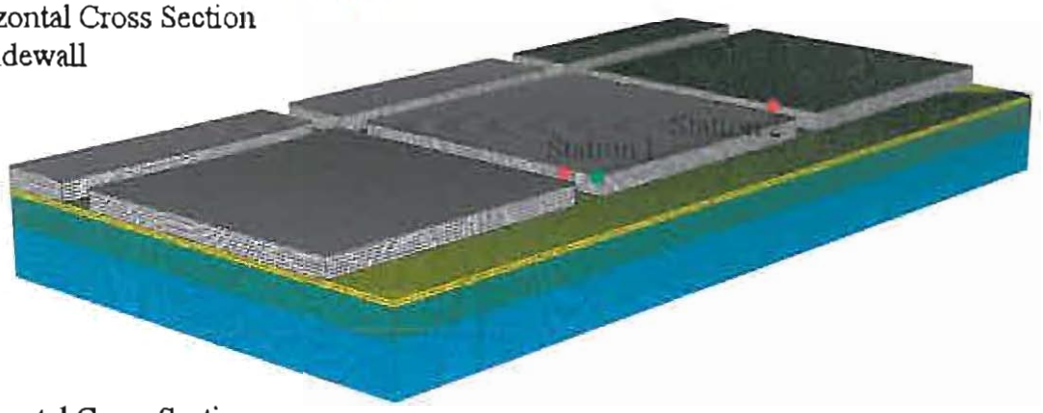

c. Horizontal Cross Section of Working Face

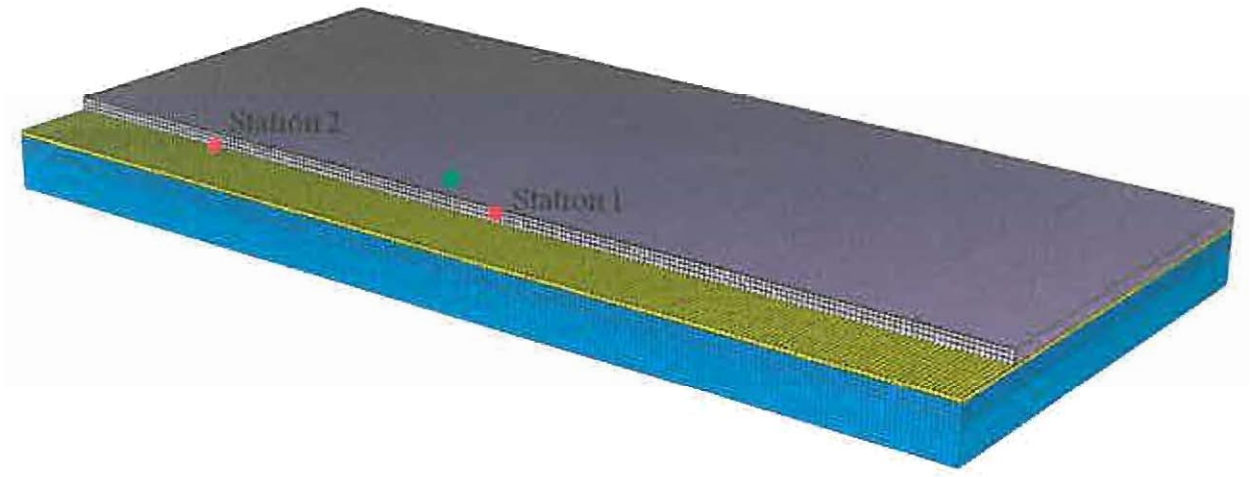

Figure 39 Cross sections of FEM models for numerical simulation of acoustic emission in mining structures

The discussion of mathematical details of the algorithm is omitted from this report for the sake of brevity. Interested readers are referred to Hilber, Hughes, and Taylor [1978] for further readings. The damping parameter used in the calculation is 0.05.

During the FEM simulation, the displacement cumulation was divided in $\Delta t = 0.1$ msec steps for the integration iteration. The entire time duration of the simulation is about 0.21 sec., which is more than sufficient for the AE signal to travel from the source to the monitoring stations. Since the upper bound of the signal frequency is 1500 Hz, the shortest period, T, of interest is 0.67 msec. The ratio of the shortest period, T, in the AE signal to time step size for integration, Δt, is 6.7, which ensures that the implicit algorithm will generate reliable results. Compared with 0.1 msec time step, the time for fracture formation is considered transient. The dynamic load of AE source, therefore, uses δ-functions:

$$F\delta(t) = \begin{cases} \pm 4\sigma_m a^2 & when\ t = 0 \\ 0 & when\ t > 0 \end{cases} \qquad \text{(Eq. 11)}$$

The calculated value of F at $t = 0$ is approximately ±1 MN. The plus/minus sign indicates the two forces acting in opposite directions.

FEM simulations of acoustic emission activities were conducted on the three preliminary models of basic mining structures. The input excitation (load) of fracture generation was applied on the disengaged nodes in the fracture surfaces as discussed earlier. The output AE activities (displacements) were obtained from two monitoring stations on each model as shown in Figure 39. There were a total of 193,056 elements for the mine panel model, 220,800 elements for the sidewall, and 508,800 elements for the model of working face. In order to save processing time, parallel implementation of the block parse solver in ABAQUS was used. The model calculation was divided among 8 CPUs, which ran 13 – 43 hours on a high performance computer at Dartmouth College for each simulation. The simulated AE signals at each monitoring station are plotted in Figure 40 for mine panel, Figure 41 for sidewall, and Figure 42 for working face. Since no field data is available at this stage, the work for model validation and modification is pending.

The FEM software, ABAQUS, is chosen for this application because of its superb interactive user interface, graphical capabilities and the proposers' past experience in using the software. In the application, the three basic elements of mining structures were simulated. The results from FEM simulation will be compared with the in-situ AE activity measurement obtained in Aim 3 for model validation/improvements and for subsequent AE signal characterization and failure criteria development. By using ABAQUS, the results of stress analysis may be easily plotted in the form of a contour plot, from which the location of the maximum stresses can be conveniently identified and evaluated. The details of finite element techniques may be found in Ziekiewicz [1971] and Hinton and Owen [1989].

4.4.2 Sub-Task 4.2 AE waveform feature classification

Since no field data is available at this time, no activity will be reported for this sub-task.

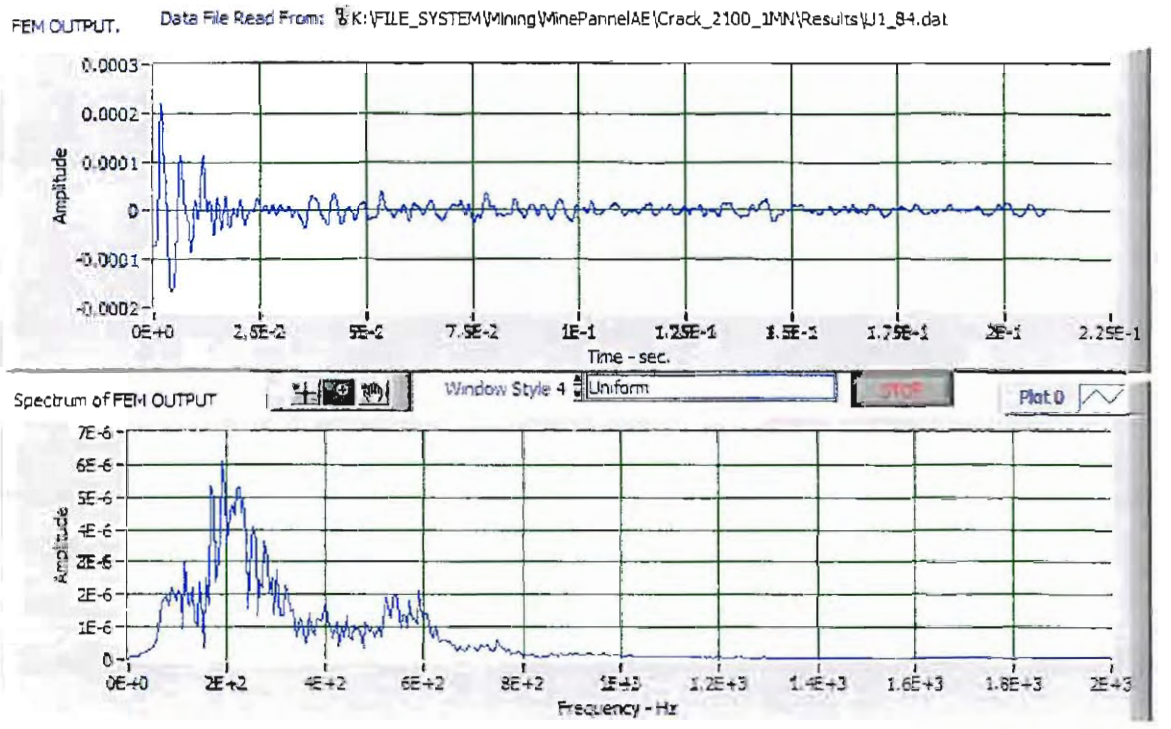

a. FEM-simulated AE activity at Station 1

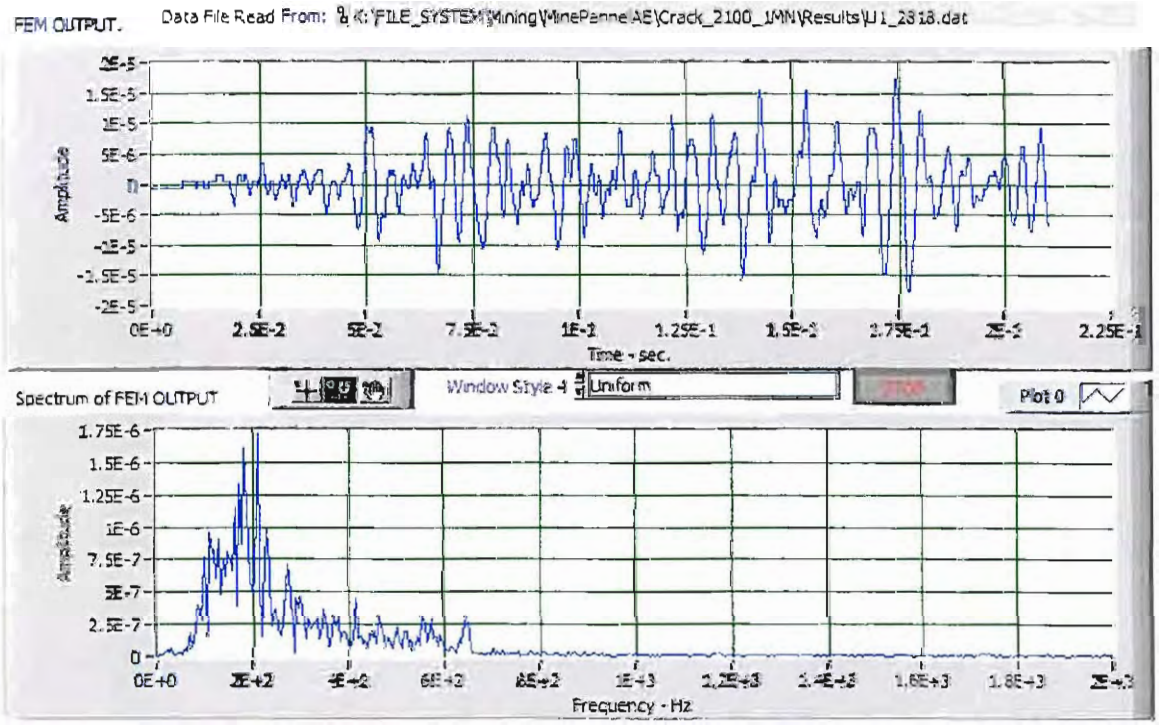

b. FEM-simulated AE activity at Station 2

Figure 40 FEM simulation of acoustic emission activity in mining structures (see Figure 39a mine panel)

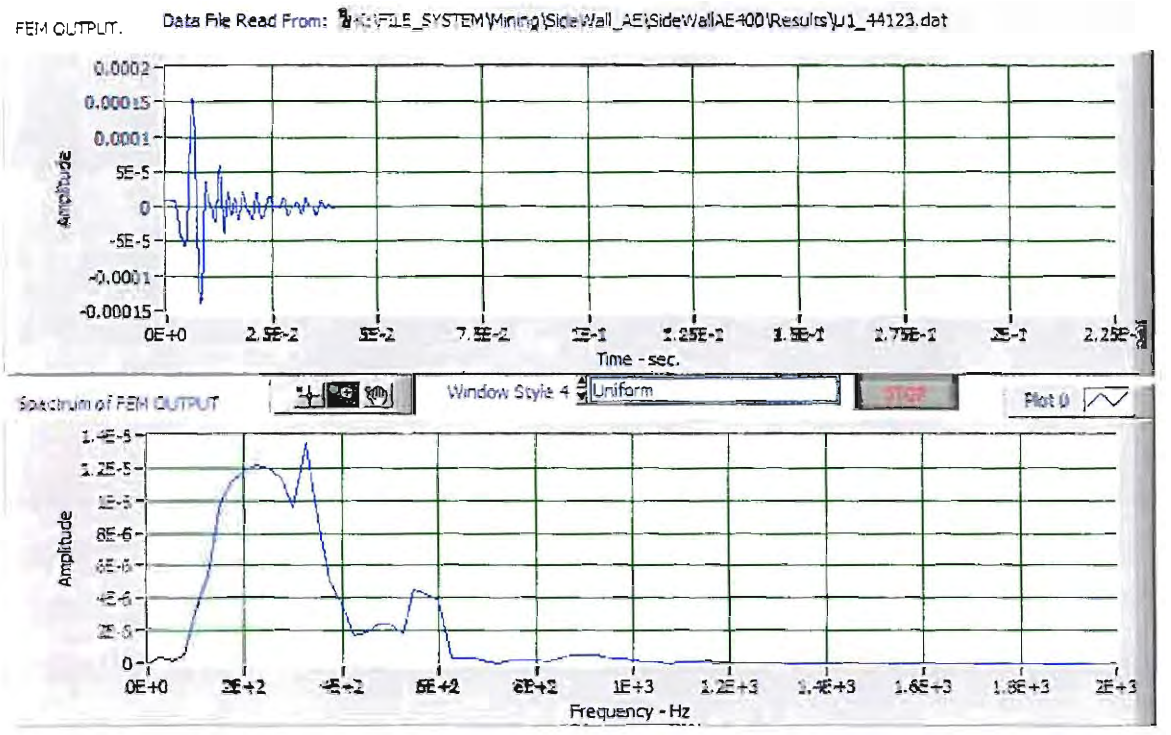

a. FEM-simulated AE activity at Station 1

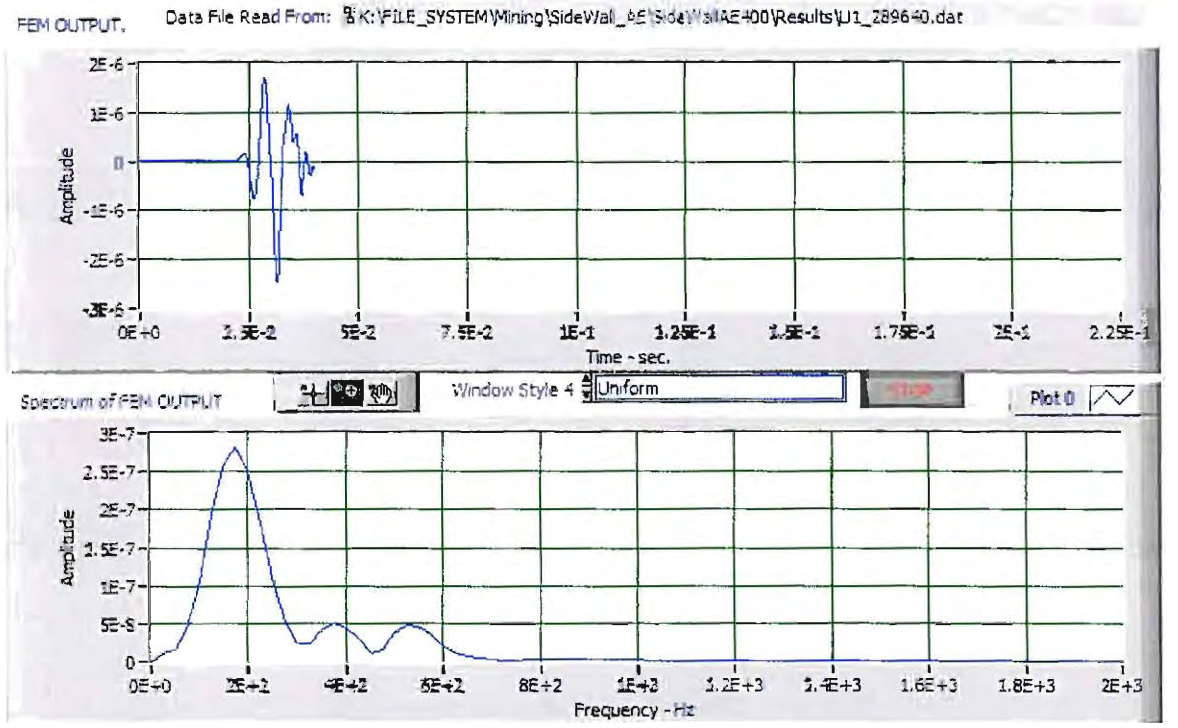

b. FEM-simulated AE activity at Station 2

Figure 41 FEM simulation of acoustic emission activity in mining structures (see Figure 39b stope sidewall, data incomplete)

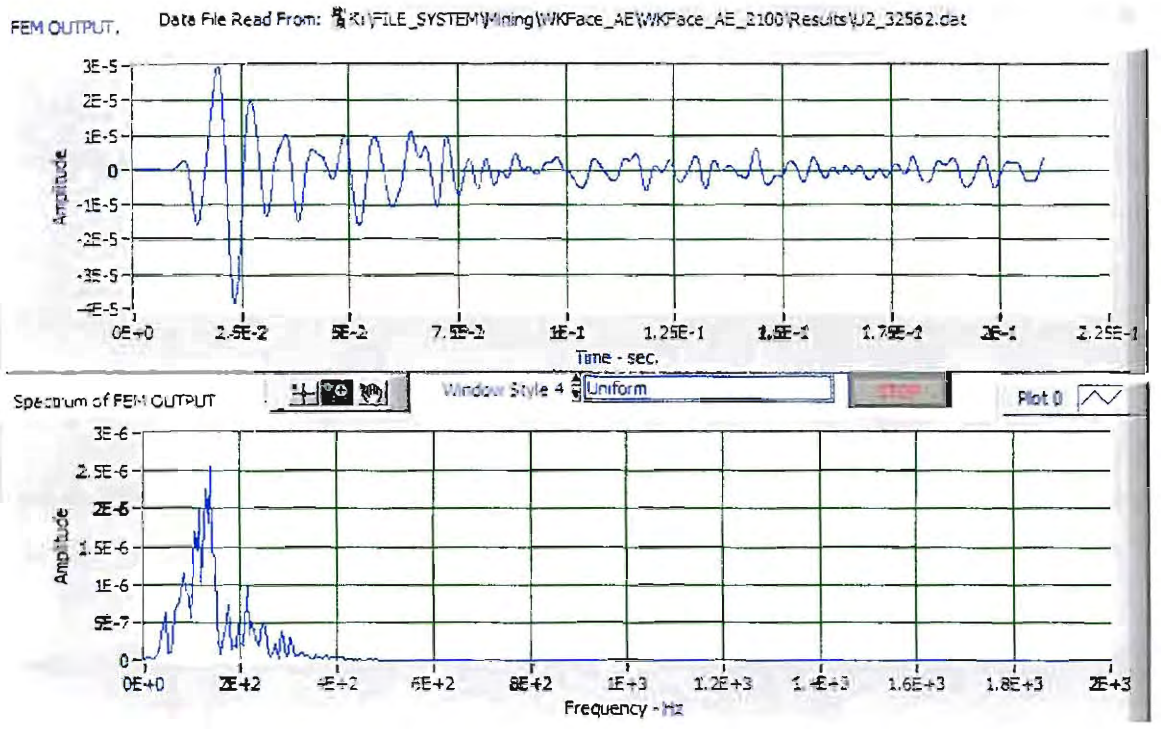

a. FEM-simulated AE activity at Station 1

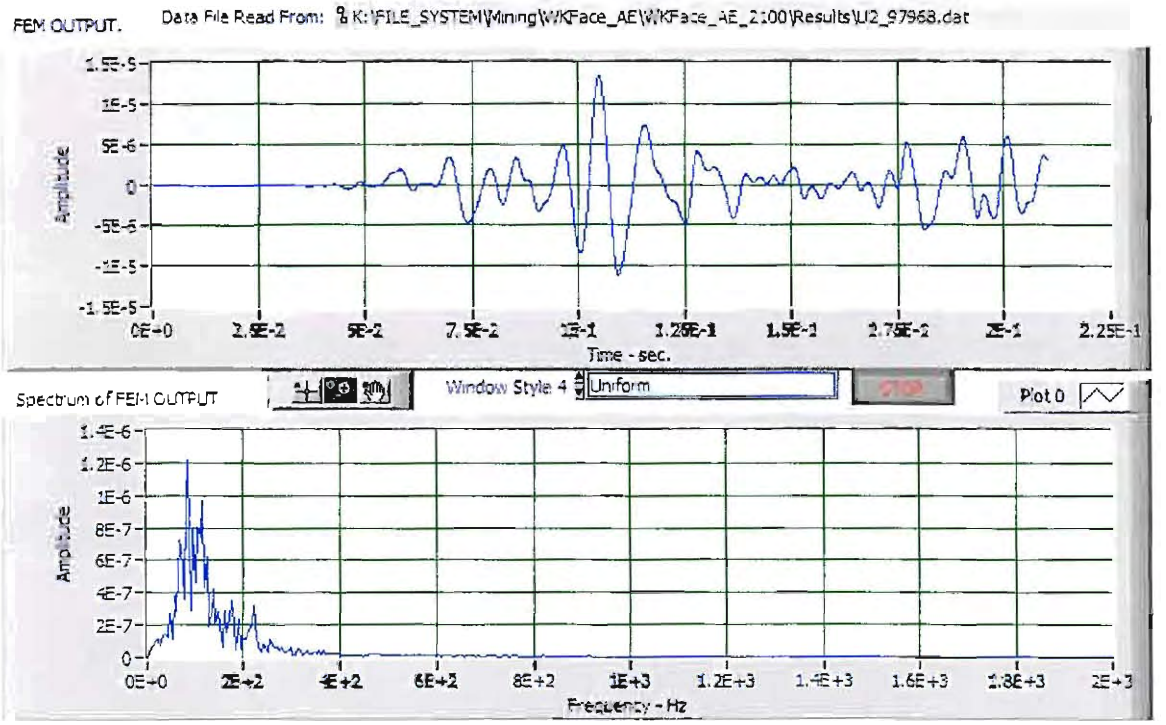

b. FEM-simulated AE activity at Station 2

Figure 42 FEM simulation of acoustic emission activity in mining structures (see Figure 39c working face)

4.5 Aim 5: System Integration and In-Situ Trial

The effort of system integration will be divided into two steps. In the first step, the entire system will be integrated in a rugged portable format suitable for use in the mining environment. All technical objectives should be met and tested. The AE criteria for instability development in mining structures should be developed and verified in field applications. After the first step, the equipment should be sellable to industrial users. The second step will further improve the functions of the instrumentation and achieve miniaturization of the equipment with the revenue derived from sales, in order to meet the requirement of individual users.

Based on this philosophy, the mine AE detector, SAFELITE-1, was configured for trial and applications. SAFELITE-1 is built in a rugged package for use in the mining environment. The block diagram of the system is shown in Figure 43. SAFELITE-1 is portable equipment consisting of two units: an optical AE detection unit and a signal processing and control unit. The optical AE detection unit contains TWM based interferometry for underground acoustic emission signal detection, a detection probe, high voltage signal modulator and a common power supply. The signal processing and control unit involves data acquisition, processing, and AI functions to perform pattern recognition analysis of the incoming AE signals and to provide display of the detection results and warning if any potential instabilities occur. These two units will be described below.

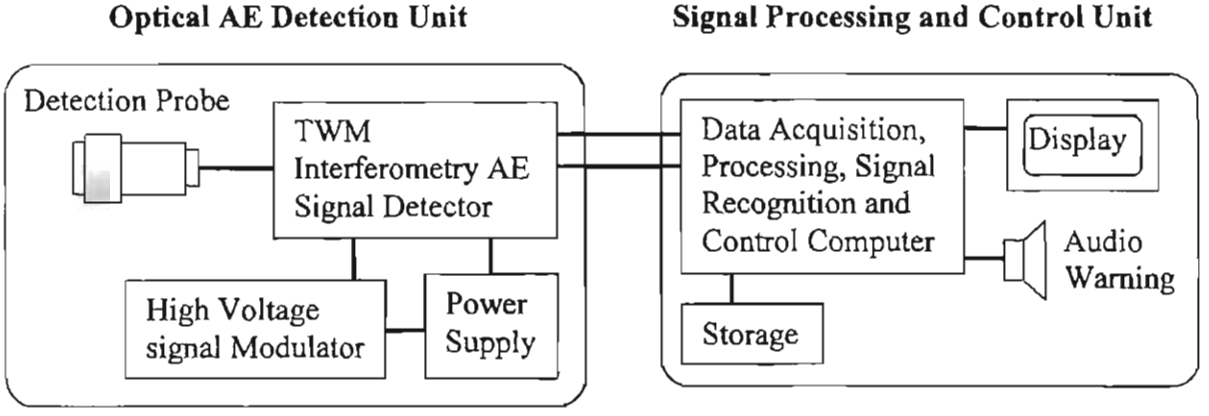

Figure 43 Assembly block diagram of SAFELITE-1 (laser based device for work site stability assessment)

Optical AE Detection Unit. The optical AE detection unit is based on TWM interferometry. The unit is assembled in a two-layer instrumentation case with the upper shelf for optical layout and the lower shelf for electronics. Figure 44 shows the block diagram for the layout of TWM interferometry assembly in SAFELITE-1 mine AE detector. This TWM interferometry was used in the Phase I study [Sun et al., 2005] and optimized in the Aim 1 effort. The operating principle has been discussed in Section 4.1. Compared with the setup shown in Figure 3, the configuration for SAFELITE-1 was slightly modified. First, several mirrors (M_1, M_2, M_3, M_6 and M_7) were introduced to redirect the laser beams in order to fit the interferometer in the limited space in the cabinet. Second, the laser beam will be projected to testing surface by a detection probe through an armored optic fiber cable. The probe is a lens set that is also responsible for collecting light

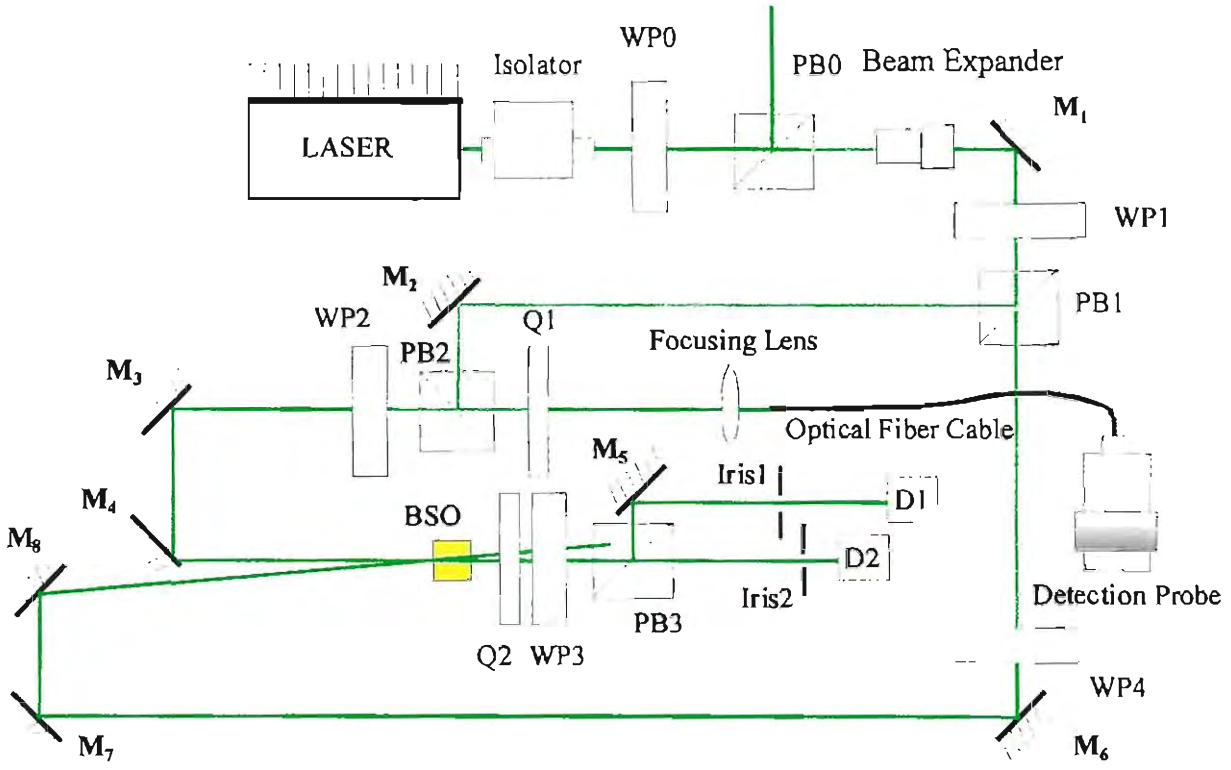

Figure 44 Layout of TWM interferometry assembly in SAFELITE-1 detection unit

Figure 45 TWM interferometry AE signal detector on top shelf of the instrument case

reflected from the testing surface. In addition to these changes, low profile fixtures were adopted in the instrumentation cabinet and an exhaust cooling fan was installed for the laser. Figure 45 shows a photograph of the TWM interferometry on the top shelf of the AE detector instrumentation case.

High Voltage Signal Modulator. The high voltage signal modulator is to provide a 3.2 KHz, 1000 to 8000 Volt (peak-peak) sinusoidal electric field across the photorefractive crystal (BSO) so that the photorefractive effect of the crystal can be enhanced. The voltage output is variable from 1000 to 8000 volts in order to provide flexibility in sensitivity adjustment for optimization of the interferometer performance.

The modulator is based on a 3.2 KHz sinusoidal function generator and a high voltage signal amplifier. It is designed to have output current capability of ±20 mA AC. The modulator consists of all solid state circuits with a slew rate greater than 150 V/μs and a large signal bandwidth from DC up to 6 KHz, as well as very low noise operation. The four-quadrant active output stage sinks or sources current into the following reactive load throughout the required output voltage range. This technique is essential for achieving the accurate output responses and high slew rates demanded by the photorefractive crystal.

The modulator also incorporates a current trip or limit that is adjustable for 0 to 20 mA using a potentiometer. When it encounters a current trip condition, the high voltage output is disabled, and a Trip Status indicator will illuminate. Since the detailed schematics of the modulator involve our collaborator's (Trek Inc., 11601 Maple Ridge Road, Medina, NY 14103) proprietary information, they will not be presented in the report. Figure 46 shows the assembly plot of the unit. The photographs of the modulator are shown in Figures 47 and 48.

Power Supply. A common power supply is required for the green laser (532 nm), high voltage signal modulator, and photo-detector in the SAFELITE-1 detection system, as specified in Table 7. The power supply is selected from the commercial market. Specifically, the OEM power unit comes from ACE series modular medical power supplies manufactured by COSEL Co., Ltd, Tayama, Japan. This modular series is specially designed for medical applications, and complies with UL2601-1/EN60601-1 safety standard. The part number for this unit is AC3-MZWK-00. The AC power input required is 85 – 264 Volts single phase source. Figure 49 shows the appearance of the power unit.

Figure 50 shows the photograph of the lower shelf of the instrumentation case with all electronics installed. Figure 51 shows the appearance of the optical AE detection unit of SAFELITE-1 mine AE detector.

Table 7 Power Requirement of the Ultrasonic Diagnostic System

No.	Voltage	Current Capacity	Description (required by)
1	+5 v	10 A	532 nm Laser (4.0 A)
2	±12 v	5 A	532 nm Laser (3.0 A)
3	±15 v	4 A	High Voltage Signal Modulator (0.5 A), Photo-Detector (300 mA)
4	+ 48 v	4 A	High Voltage Signal Modulator (2 A)

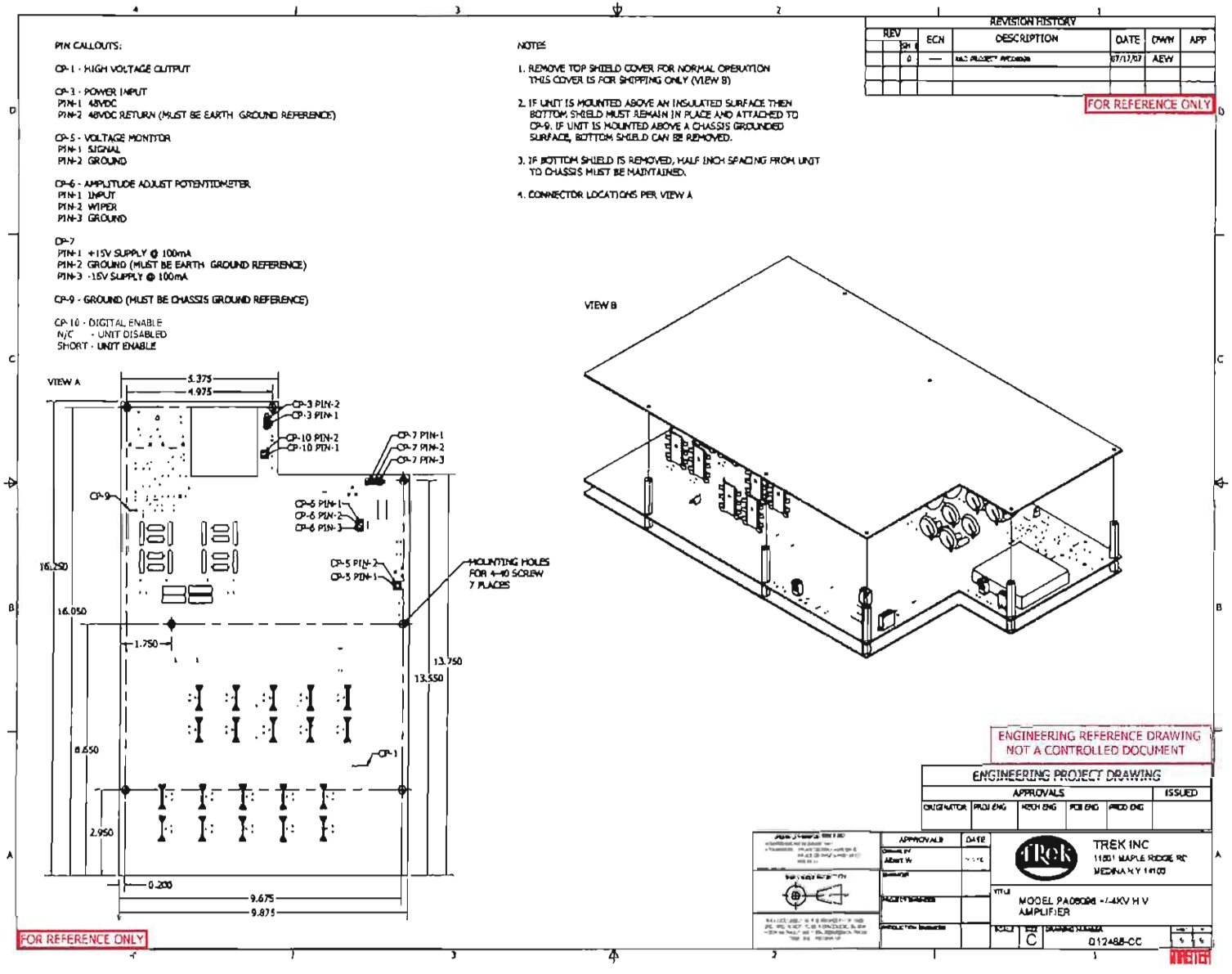

Figure 46 Assembly plot of high voltage signal modulator

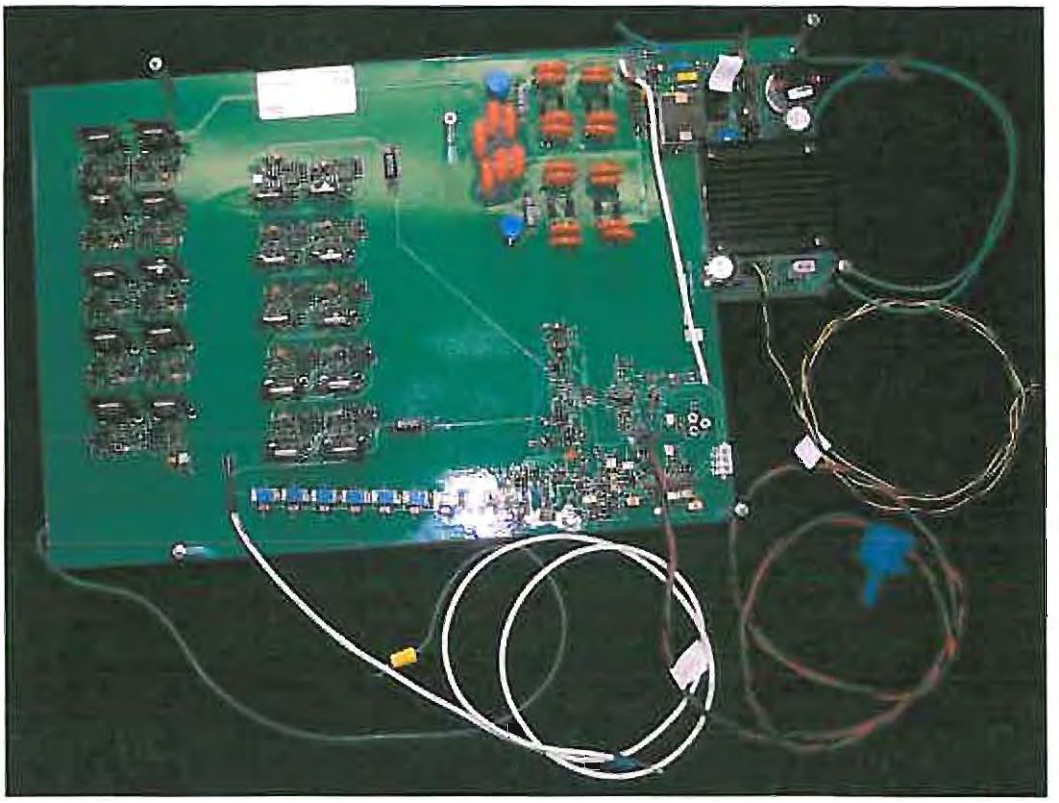

Figure 47 Photograph of the high voltage signal modulator

Figure 48 High voltage signal modulator with electro-magnetic shield

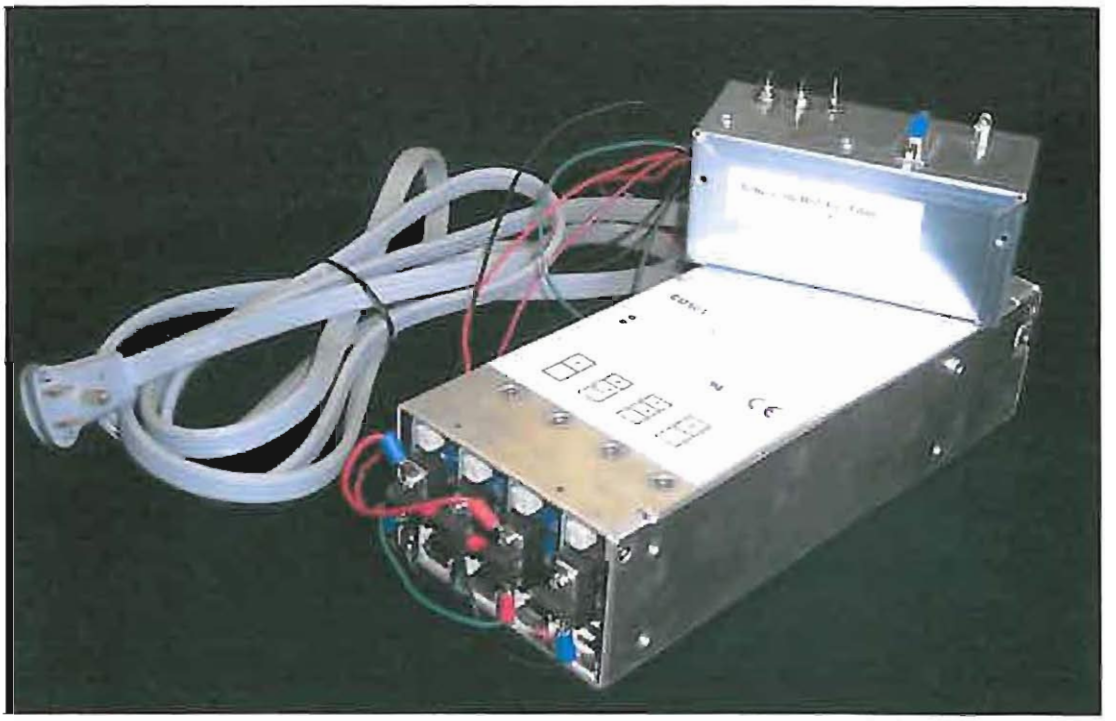

Figure 49 OEM common power supply for the AE monitoring system (manufactured by COSEL, Co., LTD, Tayama, Japan

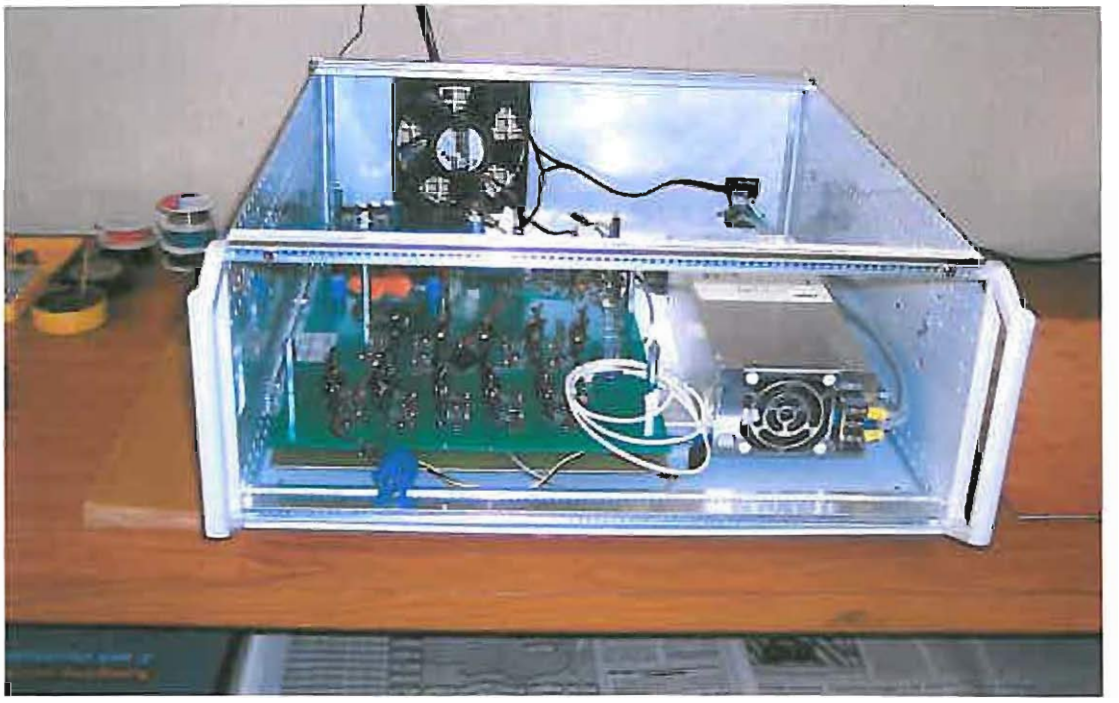

Figure 50 Power supply and high voltage signal modulator mounted on bottom shelf of instrument case

Figure 51 Optical AE detection unit of SAFELITE-1 AE monitoring system

Signal Processing and Control Unit. The signal processing and control unit is based on a panel computer mounted in a rugged carrying case for use in the mining environment. The particular computer used in SAFELITE-1 is an ACNODES Model PC2150 all-in-one super slim panel PC. PC2150 is designed mainly for industrial automation and space-constricted embedded applications. The panel PC uses touch screen as input without the need for keyboard and mouse. This is especially useful in field applications in environments such as mine sites. It also has a full size PCI slot for a data acquisition board. The panel computer is fully IBM PC compatible, operates by WINDOWS system, and provides a friendly environment for LabView software in data acquisition and processing control.

Data Acquisition. Data acquisition involves data collection and digitization. This part of the function is realized by a National Instrument PCI-5122 high resolution digitizer board. PCI-5122 has 14-bit resolution on 2 simultaneously sampled channels with ± 100 mV_{pp} to ± 10 V_{pp} range. The sampling frequency is up to 100 MHz. The data acquisition board is operated by LabView software with no additional drivers. PCI-5122 fits in the PCI slot in the panel PC 2150.

Signal Processing and Pattern Recognition. The signal processing and pattern recognition functions will be implemented by using LabView software package. LabView is a graphical programming language that has been used for data acquisition and instrument control. The LabView software package provided by National Instrument is a powerful and flexible instrumentation and analysis software programming system that incorporates intuitive user interface, instrument drivers, data processing functions, multimedia input/output and Internet capabilities for scientific and engineering applications. The software works under the

WINDOWS operating environment. The functions used in SAFELITE-1 involve: coordination of signal collection and digitization, mathematical functions, data presentation on virtual instrument, signal processing such as windowing, filtering and statistics extraction, and multimedia output. All these functions are realized by graphical block diagram. Some functions in SAFELITE-1 for pattern recognition, which cannot be found in LabView's program library, may be programmed in C-language and then interfaced to LabView. The digital audio AE monitor discussed in Section 4.1.3 is also programmed in LabView language. Figure 52 shows the LabView block diagram developed for SAFELITE-1 general instrumentation and data processing control. Figure 53 shows the virtual instrumentation and calibration panel of SAFELITE-1.

Figure 54 shows the photograph of the signal processing and control unit ready for field tests. Figure 55 is the photograph of the SAFELITE-1 AE monitoring system. At this stage, SAFELITE-1 has not been completed for field tests and failure criteria development, because one of its key parts, the optical fiber amplifier, is still under development, as discussed in Section 4.1.4.

4.6 Conclusion

This report documents the SBIR Phase II activity entitled "A Laser-Based Device for Work Site Stability Assessment" conducted by AAC International under Grant Number 2 R44 OH007662-02 and 5 R44 OH007662-03. The project was productive and fruitful, although it has not been completed because the amount of the actual work was far beyond the original estimates. Significant progress was made toward the final project goal.

The concept for instrumentation of the proposed laser device for work site stability monitoring was demonstrated in the previous Phase I project. In the Phase II effort, the instrumentation was further reduced into its prototype format suitable for field applications through system optimization, miniaturization, and cost reduction. A digital audio AE monitor was also developed and tested, which is the first reduced into practice in the field. AE signal detection by laser instrumentation was tested on rock materials. It was found that weak signal caused by low optical reflectivity of rock surfaces may seriously degrade the quality of the AE detection, therefore effort was directed to developing an optical fiber amplifier (OFA) for compensation. In preparation of field experiments on the stability monitoring system and failure criteria development based on acoustic emission, preliminary finite element models were constructed to study stress distribution around underground longwall stope and to simulate AE activities generated in the rock structures. This established a framework for the analytical part of further development for field applications. In the effort of system integration, the first generation mine AE monitor implementing the proposed laser-based AE detection concept, SAFELITE-1, has been assembled with major functions tested. At this stage, SAFELITE-1 has not been completed for field tests and failure criteria development, because one of its key parts, the optical fiber amplifier, is still under development.

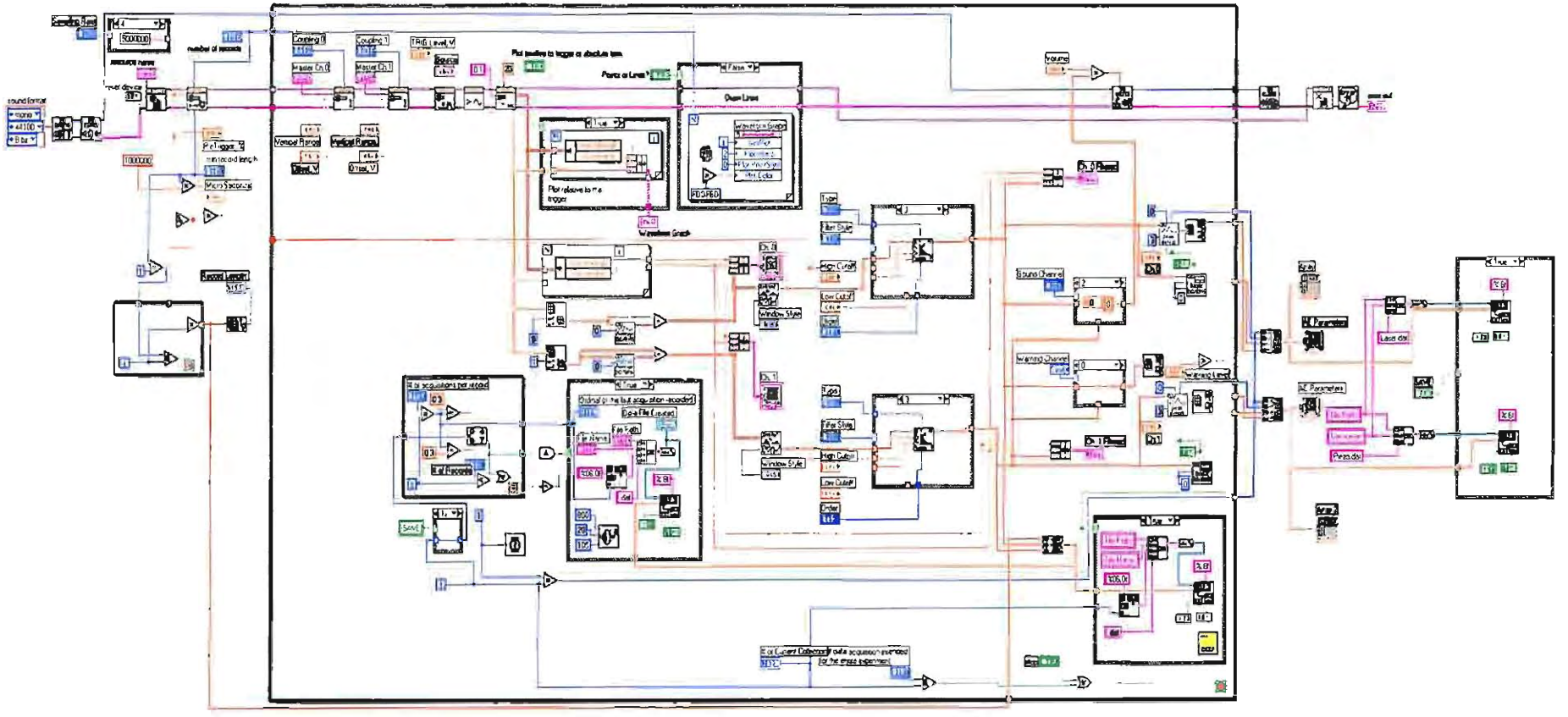

Figure 52 Block diagram of software based on LabView virtual instrument for SAFELITE-1 signal processing and control unit

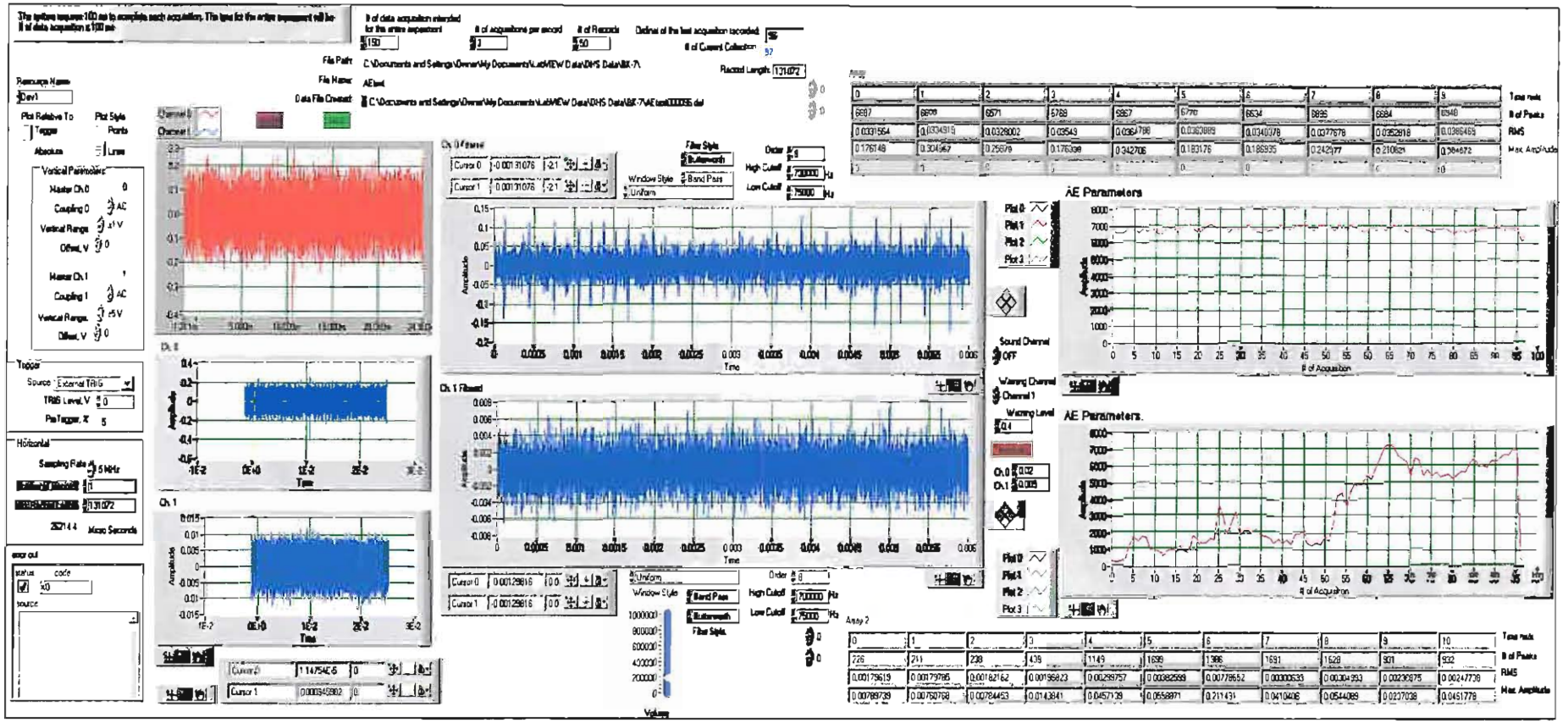

Figure 53 SAFELITE-1 instrumentation calibration panel using LabView virtual instrument on computer screen

Part 5: LITERATURE CITED

Allain JY, Monerie M, Poignant H: [1990] Room temperature CW tunable green upconversion holmium fibre laser. Electron. Lett. 26:261-263.

Carolan TA, Reuben RL, Barton JS, Jones JDC: [1997] Fiber-optic Sagnac Interferometer for Noncontact Structural Monitoring in Power Plant Applications. *Applied Optics*, 36(1), 1997

Dahlen FA, Tromp J [1998] Theoretical Global Seismology. Princeton (NJ): Princeton University Press.

Fan TY: [1996] Diode-Pumped Solid-State Lasers. *Laser Sources and Applications, Proceedings of the 47th Scottish University Summer School in Physics*, (eds. A Miller, DM Finlayson P Osborne, Institute of Physics Publishing, Philadelphia.

Hardy, HR: *Acoustic Emission/Microseismic Activity: Principles, Techniques and Geotechnical Applications*. A.A.Balkema Publishers, Tokyo.

Hilber HM, Hughes TJR, Taylor RL: [1978] Collocation, Dissipation and 'Overshoot' for Time Integration Schemes in Structural Dynamics. *Earthquake Engineering and Structural Dynamics*, Vol. 6, 1978.

Hinton E, Owen, DRJ: [1989] *Finite Element Programming*, Academic Press, San Diego

Jaeger JC, Cook NGW: [1969] *Fundamentals of Rock Mechanics*, Methuen, London.

Johnson AJ: [1987] Acoustic Emissions at an Opening Crack. Proc. of the Review of Progress in QNDE 7, (eds. DO Thompson, DE Chimenti) Plenum Press, New York, pp1503-1511.

Jumikis AR: [1983] *Rock Mechanic*, Trans Tech Publications, Clausthal-Zellerfeld, Germany.

Müller L: [1974] *Rock Mechanics*, Springer-Verlag, New York.

Murray TW, Krishnaswamy S: [2001] Multiplexed Interferometer for Ultrasonic Imaging Applications. *Optical Engineering*, 40(7).

Pepper DM: [1997] The Emergence of Nonlinear Optics in the Factory. *Optics and Photonics News*, May, 1997.

Petrov MP, Sokolov IA, Stepanov SI, Trofimov GS: [1990] Non-Steady-State Photo-Electromotive-Force Induced by Dynamic Gratings in Partially Compensated Photoconductors. *J. Appl. Phys.*, 68(5), Sept. 1990.

Quimby RS, Zheng B: [1992] New Excited-State Absorption Measurement Technique and Application to Pr^{3+} Doped Fluorozirconate Glass. Appl. Phys. Lett. 60:1055-1057.

Sun X, Wang J, Silliman R: [2005] A Laser-Based Device for Work Site Stability Assessment. CDC-NIOSH SBIR Phase I Final Report, Grant#1 R43 OH007662-01A1.

Tropper AC, Carter JN, Lauder RDT, Hanna DC, Davey ST, Szebesta D: [1994] Analysis of Blue and Red Laser Performance of the Infrared-Pumped Praseodymium-Doped Fluoride Fiber Laser. J. Opt. Soc. Am. B 11(5):866-893.

Xie P, Gosnell TR: [1995] Room-Temperature Upconversion Fiber Laser Tunable in the Red, Orange, Green, and Blue Spectral Regions. Optic Letters Vol. 20, No. 9, 1014-1016.

Zhou Y: [2004] *Multiplexed Two-Wave Mixing Interferometry*, PhD Thesis, Northwestern University.

Ziekiewicz OC: [1971] *The Finite Element Method in Engineering Science*, McGraw-Hill, New York.

VI. PUBLICATIONS

A paper entitled "Non-Contact Detection of Acoustic Emission Signals from Rock Structures" authored by Xiaoqing Sun, is accepted and will be presented in *43rd US Rock Mechanics Conference* (June 28, 2009)

It is also intended to publish another paper entitled "FEM Simulation of Acoustic Emission Activity in Underground Mining Structures" authored by Xiaoqing Sun in the near future in *International Journal of Rock Mechanics and Mining Sciences.*

Both papers listed above are resulted from this SBIR project.

VII. INCLUSION OF GENDER AND MINORITY STUDY SUBJECT

No human subject is involved in this research project.

VIII. INCLUSION OF CHILDREN

No human subject is involved in this research project.

IX. MATERIALS AVAILABLE FOR OTHER INVESTIGATORS

All technical information presented in this report and referenced data will be accessible for government use. Industrial users should contact *AAC International, 60 Mechanic Street, Lebanon, NH 03766, and Phone (603)448-6177.*